THE EFFECT OF MATERIAL STRAIN RATE SENSITIVITY ON THE SHOCK DEFORMATION OF AN ALUMINUM CORRUGATED CORE

A Thesis Submitted to
The Graduate School of Engineering and Sciences of
İzmir Institute of Technology
in Partial Fulfillment of the Requirements for the Degree of

MASTER OF SCIENCE

in Mechanical Engineering

by
İlker CANBAZ

June 2018
İZMİR

We approve the thesis of **İlker CANBAZ**

Examining Committee Members:

_____

Prof. Dr. Mustafa GÜDEN
Department of Mechanical Engineering, İzmir Institute of Technology

_____

Prof. Dr. Yeliz PEKBEY
Department of Mechanical Engineering, Ege University

_____

Assoc. Prof. Dr. Erdal ÇETKİN
Department of Mechanical Engineering, Izmir Institute of Technology

_____

Assoc. Prof. Dr. İzzet ÖZDEMİR
Department of Civil Engineering, Izmir Institute of Technology

_____

Assist. Prof. Dr. Selçuk SAATCI
Department of Civil Engineering, Izmir Institute of Technology

04 June 2018

_____

Prof. Dr. Mustafa GÜDEN
Supervisor, Department of
Mechanical Engineering
İzmir Institute of Technology

_____

Prof. Dr. Alper TAŞDEMİRCİ
Co-Supervisor, Department of
Mechanical Engineering
İzmir Institute of Technology

_____

Prof. Dr. Metin TANOĞLU
Head of the Department of
Mechanical Engineering

_____

Prof. Dr. Aysun SOFUOĞLU
Dean of the Graduate School of
Engineering and Sciences

ACKNOWLEDGEMENTS

First of all, I would like to express my deepest thanks to my supervisor Prof. Dr. Mustafa GÜDEN for his for instructive comments, patience and precious guidance during the entire thesis study. Secondly, I would like to thank to my co-advisor Prof. Dr. Alper TAŞDEMİRCİ for his support.

I owe a debt of gratitude to Mustafa Kemal SARIKAYA for all his technical support and contributions to my thesis study and also his friendship. Thanks to Dynamic Testing and Modelling Laboratory's members of Muhammet ÇELİK, Mesut BAYHAN Semih Berk SEVEN for both their collaboration and friendship.

I would also thanks to my manager Musa ÖZÇELİK at ZF Lemförder Aks Modülleri Sanayi ve Ticaret A.S. for his support and understanding attitudes during this period.

Last but not least, I would like to express my gratitude to my family; my father Fuat CANBAZ and my mother Ayşe CANBAZ, for being supportive and promotive. Their presence makes it easier to overcome all challenges.

ABSTRACT

THE EFFECT OF MATERIAL STRAIN RATE SENSITIVITY ON THE SHOCK DEFORMATION OF AN ALUMINUM CORRUGATED CORE

The effect of the material model on the crushing behavior of a layered 1050 H14 aluminum corrugated sandwich structure was investigated numerically as function of velocity (0.0048, 20, 60, 150 and 250 m s^{-1}) using three different material models; elastic-perfectly plastic (model I), elastic-strain hardening (model II) and elastic-strain and strain rate hardening (model III). Three-dimensional finite element models were developed in the explicit finite element code of LS-DYNA. Between 0.0048 m s^{-1} and 20 m s^{-1}, the numerically calculated stresses at the impact and distal end were almost the same and in equilibrium, showing a "quasi-static homogenous mode". The deformation mode at 60 m s^{-1} was a "transition mode" and between 150 and 250 m s^{-1} a shock mode in which the layers were crushed sequentially. The numerical study showed that the strain and strain rate hardening models tended to induce non-sequential layer crushing. The collective layer crushing was also more pronounced in the material model II and III than the material model I. For low strain hardening aluminum alloys and similar materials, the effect of strain hardening in increasing plateau stress was more significant than the strain rate hardening at the quasi-static velocity, while both strain hardening and strain rate hardening effect increased with increasing velocity. The stress reduction by the inclusion of imperfections however declined with the velocity since the samples started to deform near the impact end as the velocity increased.

ÖZET

DALGALI BİR ALÜMİNYUM DOLGU YAPISINDA GERİNİM DUYARLILIĞININ ŞOK DEFORMASYONUNA ETKİSİ

Çok katmanlı 1050 H14 alüminyum dalgalı sandviç yapının malzeme modelinin, ezilme davranışı üzerindeki etkisi nümerik olarak incelendi. Farklı hızlarda (0.0048, 20, 60, 150 ve 250 m s^{-1}) üç farklı malzeme modeli, elastik-mükemmel plastik (model I), elastik-gerinim sertleşmesi (model II), elastik gerinim ve gerinim oranı sertleşmesi (model III) kullanılarak araştırma gerçekleştirildi. LS-DYNA programının açık dinamik sonlu eleman kodu kullanılarak üç boyutlu sonlu eleman modelleri geliştirildi. 0.0048 m s^{-1} ve 20 m s^{-1} arasında darbe ucundan ve uzak uçtan nümerik olarak hesaplanıp elde edilen stres değerlerinin neredeyse eşit olması bu hız aralığındaki deformasyon modunun yarı statik homojen mod olduğunu gösterdi. Deformasyon modu 60 m s^{-1} hızda geçiş modu iken 150 ve 250 m s^{-1} arasında şok modu olup numune katmanları ardışık olarak ezilmiştir. Elastik-gerinim sertleşmesi (model II), elastik gerinim ve gerinim oranı sertleşmesi (model III) modelleri ardışık olmayan katman ezilmesi eğilimi göstermiştir. Ayrıca toplu katman ezilmesi durumu II ve III numaralı malzeme modellerinde I numaralı malzeme modeline göre daha fazla meydana gelmiştir. Düşük pekleştirmeli alüminyum ve benzeri malzemeler için yarı statik hızda gerinim sertleşmesinin plato geriliminin artması üzerindeki etkisi, gerinim sertleşmesi oranının etkisinden daha fazladır. Hızın artmasıyla birlikte gerinim sertleşmesi ve gerinim sertleşmesi oranının etkisi artmaktadır. Ayrıca hız arttıkça numune darbe ucuna yakın yerden deforme olmaya başladığından kusurlu katmandan kaynaklanan ilk ezilme stresindeki düşüş miktarı da azalır.

TABLE OF CONTENTS

LIST OF FIGURES

Figure **Page**

CHAPTER 1

DYNAMIC DEFORMATION OF METALLIC CELLULAR STRUCTURES

Metallic cellular structures refer to wide range of light-weight structures that include aluminum, titanium and steel based open and closed cell foams, aluminum honeycombs, aluminum and steel corrugated and lattice structures. These structures deform under compression loads by the collapse/failure of the thin walls of metal sheet. The collapse for example in an Al closed cell foam occurs by the buckling and extension of cell walls. The metallic foams and honeycombs as being widely used examples to metallic cellular structures exhibit the characteristics compression stress-strain behavior, composing of an elastic region, a nearly-constant plateau stress region and a steeply-rising stress region after a critical strain referred to as the densification strain. The steeply-rising stress region is usually concave-up, leading to the development of a shock stress when the velocity of deformation is above critical velocities, known as the velocity for shock formation.

The pioneering study on the shock formation in cellular structures was by Reid and Peng in 1997 [1]. Cylindrical wood specimens with and without backing masses were launched between 30 and 300 m s^{-1} to the end of a Split Hopkinson Pressure Bar (SHPB) incident bar. The crushing stress was measured by means of strain gages mounted on the incident bar. The stress enhancement factor defined as the ratio of the dynamic initial crushing stress to the quasi-static initial crushing stress was reported in the same study to increase with increasing the impact velocity. A rate independent rigid, perfectly plastic, locking (r-p-p-l) material shock model based on quasi-static crushing stress and densification strain was then developed [1]. The initial crushing stress of the samples tested transverse to the wood grains increased significantly with increasing velocity and agreed well with the r-p-p-l model predictions. While, the initial crushing stress of the samples tested along the wood grains increased more substantially than the r-p-p-l model prediction, with the stress enhancement factors between 2 and 3. The enhancement of the initial crushing stress of the samples tested along the wood grains was ascribed to the micro-inertial effect which was also effective in the samples tested transverse to the wood

grains [1]. Afterwards, different models basing on the r-p-p-l model have been also developed including elastic-perfectly-plastic-rigid (e-p-p-r) model [2], rigid, softening, hardening and elastic, softening, hardening material models [3] and strain hardening r-p-p-l model [4]. All these models have been developed to modify the r-p-p-l model and predict the cellular structure's dynamic response more precisely.

1.1. Rigid, Perfectly Plastic, Locking (R-P-P-L) Material Shock Model

In the shock stress formation, the initial crushing (crush band initiation) starts from the impact end and proceeds to the distal end by the progressive and sequential formation of crush bands, dividing the deforming sample in two distinct regions; crushed, densified and elastically-deformed. In the crushed and densified region, the local strain attains the densification strains and in the elastically deformed region the strain is at the elastic strain or yield strain. In the r-p-p-l model, the crushed and densified region attains a stress of σ^* and a densification strain of ε_d and the elastically deformed region attains a stress of σ_p (Figure 1.1). In Figure 1.1, u is the displacement, h is the length of the densified region, x is the uncrushed length, x_o is the initial length of the region crushed region, ρ is the density of the crushed region, ρ_o is the initial density and l_o is the initial length of the cellular sample. Two impact tests may be considered: direct impact test and Taylor-like impact test. In the direct impact test, a rigid rod with a mass of M is directly fired with a velocity of v_o to the standing cellular sample (Figure 1.2(a)) and in the Taylor-like impact test a cellular projectile with a backing mass of M is fired to a fixed wall at an initial velocity of v_o (Figure 1.2(b)). Applying mass and momentum conservations between crushed and uncrushed (elastic) regions and the Newton's second rule to the uncrushed section, the following relations can be determined for the shock stress formation sequentially in the direct impact and Taylor-like impact tests as function time,

$$\sigma^*(t) = \frac{\left(\frac{M}{A_o}\right)^2 \left(\sigma_p + \frac{\rho_o}{\varepsilon_d} {v_o}^2\right)}{\left(\frac{M}{A_o} + \frac{\rho_o u}{\varepsilon_d}\right)^2} \tag{1.1}$$

$$\sigma^*(t) = \sigma_p + \frac{\rho_o}{\varepsilon_d}\left[v_o^2 + \frac{2\sigma_p \varepsilon_d}{\rho_o} ln\left(1 - \frac{\rho_o A_o u}{M^* \varepsilon_d}\right)\right] \tag{1.2}$$

For both type of tests, the initial peak stress ($\sigma_i{}^*$) is

$$\sigma_i{}^* = \sigma_p + \frac{\rho_o}{\varepsilon_d} v_o{}^2 \tag{1.3}$$

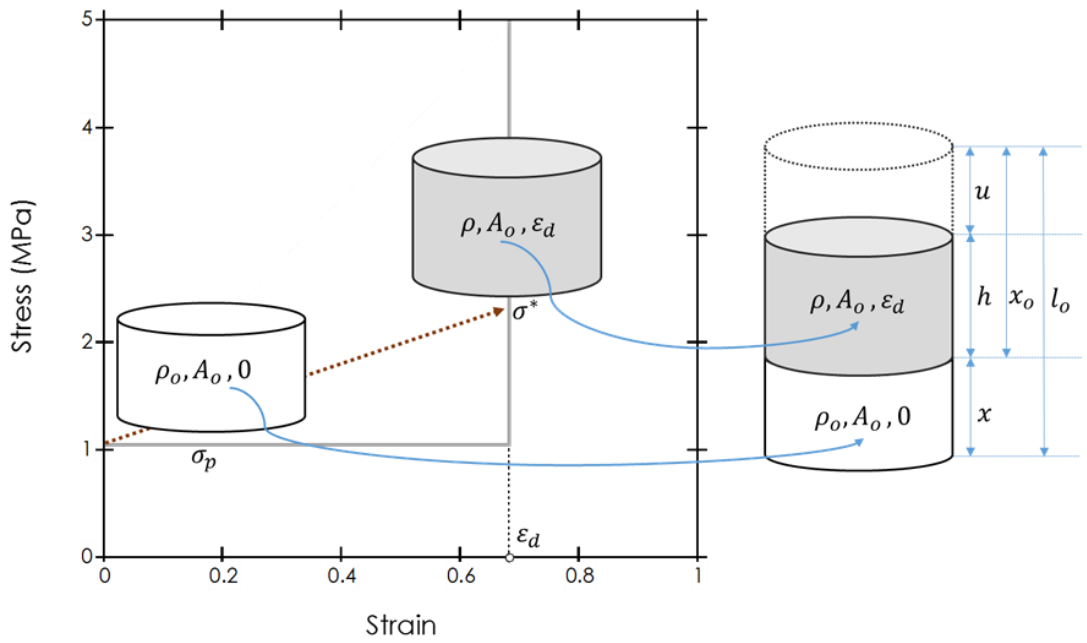

Figure 1.1. The schematic drawing of the r-p-p-l model stress-strain behavior and the crushed and uncrushed regions of a cellular sample

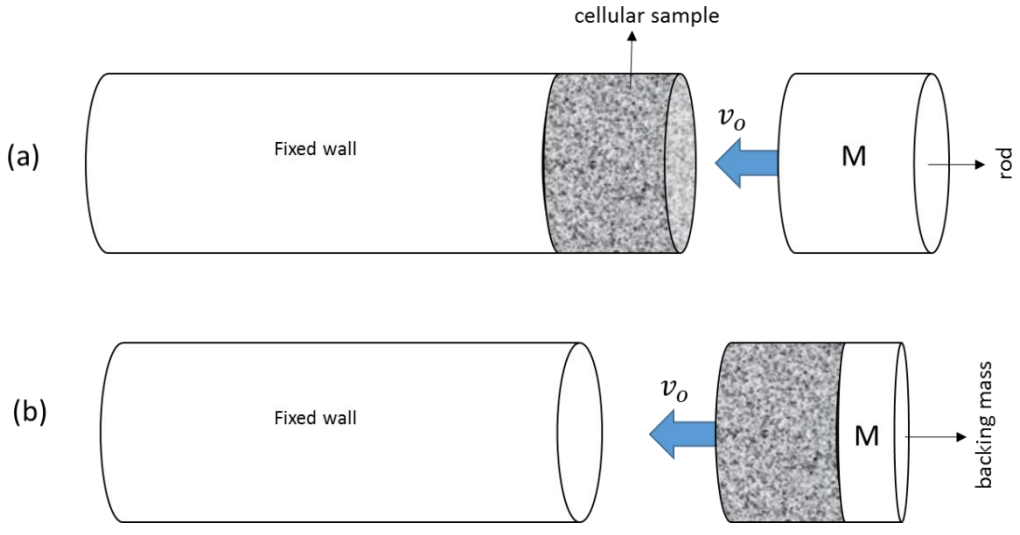

Figure 1.2. Two types of test configurations: (a) direct impact and (b) Taylor-like impact test

1.2. The Strain Rate Sensitivity of Cellular Structures

The strain rate sensitivity of cellular structures may be due to (1) the strain rate sensitivity of cell wall material, (2) compressed or entrapped air in deforming cells, (3) micro-inertia and (4) inertia or shock. The strain rate sensitivity of cell wall material affects the dynamic crushing stress of cellular structures at increasing velocities [5, 6]. However, the effect of strain rate sensitivity is usually ignored because Al and its alloys are known to have no or negligible strain rate sensitivity. During the dynamic test, the entrapped gas interior of closed cells has not enough time to escape through the existent micro cracks on cell walls. The entrapped air increases the compression stress at increasing loading rates. The stress increase due compressed air in an Al foam with a relative density of 0.2 was calculated 0.2 MPa, which can be ignored especially at high velocities [7]. The contribution of trapped air to the dynamic strength was however reported as much as 50% of the dynamic compressive strength for a relatively low density Al foam (4%) [8].

The energy absorbing cellular structures are considered in two types: Type I and Type II [9, 10]. Type I structure has a flat-topped load-deflection curve, while Type II structure has an initial peak load after which the load decreases gradually as seen in Figure 1.3. Examples of Type I and Type II structures are the lateral and axial crushing of circular thin-walled tubes, respectively. Type II structures have shown to be more sensitivity to impact velocities than Type I structures [10]. The detected strain rate dependent crushing stress of aluminum honeycombs is ascribed to the micro-inertia effect in the successive folding process [11]. The micro-inertia effect was also found in the axial crushing of square thin-walled Al extrusions [12], closed-cell aluminum foams (at different strain rates from 3.33×10^{-5} s^{-1} to 1.6×10^{-1} s^{-1}) [13], PVC foams and end-grain balsa wood (a wide range of strain rates ranging from 10^{-4} s^{-1} to 4×10^{3} s^{-1}) [14]. Both micro-inertia and strain rate sensitivity may be effective in increasing the dynamic stress. For example, the increased initial peak and plateau stress of a Ni/Al foam with the strain rate were attributed to the both the cell wall material strain rate sensitivity and micro-inertia [6]. The effectiveness of micro-inertia depends on the geometry of the structure which determines deformation mode. The inertial stabilization less affected Y-frame structure (bending dominated) by comparison with V-frame (stretching dominated) [15]. Two phases of the wall bending are considered: the plastic compression of the structure and

the rotations of plastic hinges. It was proposed that the inertia was dominant in the first phase, while the strain rate sensitivity was in the second phase [9]. Therefore, the elastic-plastic material behavior and inertia effects were both considered in determining the initial peak load. It was further reported in another study that inertia and strain rate were equally effective in Type II structures [16].

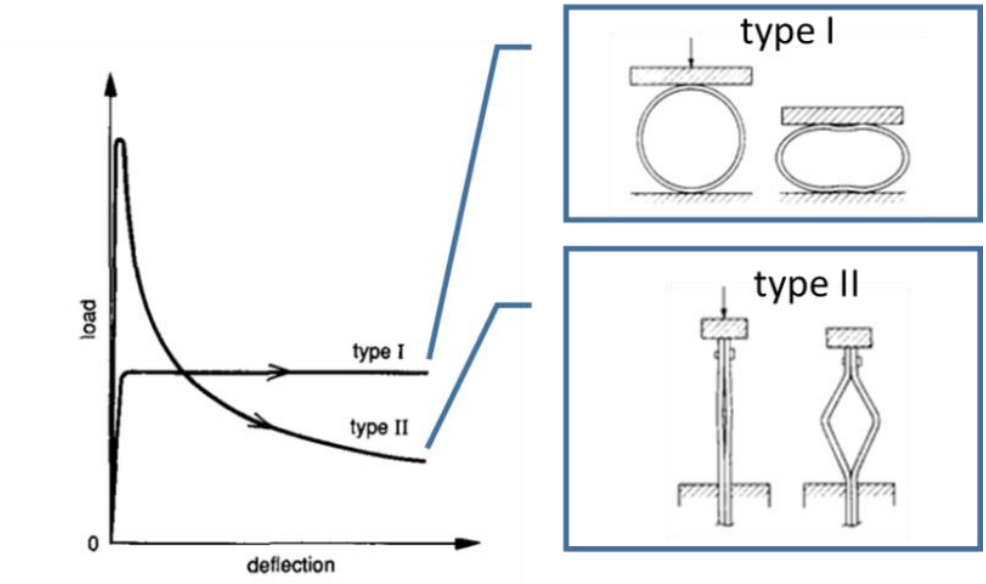

Figure 1.3. Load-deflection curves of type I and II and deformation modes

The shock deformation starts above a critical velocity [17, 18]. The shock mode was observed in the impact testing of wood [1, 3], urethane foam [19], aluminum open and closed cell foams [2, 7, 20-25], aluminum honeycomb [18] and multilayer corrugated structures [26]. In this mode, the stress developed at the impact end is far greater than that at the distal end and the difference between them increases as the impact velocity increases. The recent studies have also shown that the densification strain also increases with increasing impact velocity as similar with the crushing stress [16, 18, 27, 28].

1.3. A Concise Review of Previous Studies on the Dynamic Deformation of Cellular Structures

The experimental and numerical studies on the dynamic compressive behavior of cellular structures have been reviewed recently [29]. Therefore, the related key properties along with the limited number of studies of the dynamic deformation of honeycombs and aluminum foams will be shortly reviewed in this section.

The out of plane quasi-static and dynamic crushing of aluminum honeycombs were experimentally investigated by Wu and Jiang [30] up to 20 m s^{-1}, Zhao and Gary [31] up to 28 m s^{-1}, Harrigan et al. [32] up to ~300 m s^{-1}, Zhao et al. [11] up to 45 m s^{-1} and Tao et al. [33] up to 19 m s^{-1}. The increase in the dynamic crushing stress as compared with quasi-static stress at relatively low velocities was 74% in ref. [30], 40% in ref. [31] and 38 to 57% in ref. [33], while the dynamic crushing stress increased 10 times of the quasi-static stress value at a high velocity, 300 m s^{-1} [32]. The excessive increase in the dynamic crushing stress at high velocities is due to the shock formation. On the other side, the reported lack of stress enhancement in the in-plane-direction up to 28 m s^{-1} [31] simply indicates a Type-I behavior in this direction. Zheng et al. [34], Liu et al. [35] and Zou et al. [18] investigated the dynamic crushing behavior of 2D cellular structures numerically. The results of these studies indicated three deformation modes of regular and irregular honeycombs depending on the impact velocity as seen in Figures 1.4(a) and (b). At relatively low impact velocities, the deformation proceeds with the random collapse of weak shear bands, called the quasi-static mode. At intermediate velocities, the deformation proceeds with the localized shear and transverse bands, called the transition mode. Lastly, at high velocities where the inertial effects dominate the deformation the deformation proceeds with layer-wise collapse of transverse bands, called the dynamic or shock mode. The effect of micro-inertia was shown to be weak for Voronoi structures at high velocities and the strain rate sensitivity of the cell wall material contributed little to the increased plateau stress at increasing velocities [35]. It was also shown that the increased compressive stress in the in-plane direction of honeycomb at increasing impact velocities induced higher densification strains and longer plateau stresses [18]. The densification strain increased as the velocity increased and reached a limit which was 15% higher than that of the quasi-static value when a steady-shock front formed. It was also shown that the r-p-p-l model overestimated the crushing stresses [18]. This was partly

attributed to the constant densification strain used in the r-p-p-l model calculations in Eqns. 1.1, 1.2 and 1.3. The numerical results also showed that the strain rate played an important role in the dynamic enhancement of metallic honeycombs at relatively low velocity regime. The FE analysis on the crush band initiation and wave trapping in the impact of an aluminum honeycomb in in-plane direction showed that stress enhancement with increasing impact speed was mainly due to the translational micro-inertia and not due to the micro-rotational inertia [36]. The stress enhancement for a uniaxial stress state was found to start at about 10 m s^{-1} and above this critical velocity, crush bands initiated at the impact surface, while at lower speeds the location of the initial crush band was determined by the distribution and extent of initial imperfections.

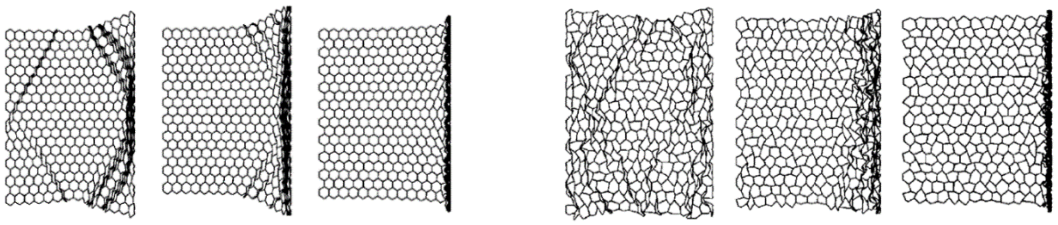

(a) (b)

Figure 1.4. Three patterns of a regular honeycomb crushed in the in-plane direction sequentially in the picture at 5, 20 and 80 m s^{-1}; (a) ordered and (b) disordered honeycomb structure

The dynamic compression and direct impact behavior of aluminum alloy foams were investigated by Deshpande and Fleck [7] between 10^{-3} and 5000 s^{-1} (Alulight and Duocel), Hall et al. [37] between 10^{-3} s^{-1} and 2000 s^{-1} (6061, powder metallurgy), Radford et al. [38] between quasi-static velocity and 500 m s^{-1} (Alporas), Tan et al. [17, 39] between 10 and 210 m s^{-1} (Hydro/Cymat), Zhao et al. [40] up to 14 m s^{-1} (IFAM and Cymat), Elnasri et al. [24] and Pattofatto et al. [41] up to 55 m s^{-1} (Alporas) Barnes et al. [16] between 20 and 160 m s^{-1} (open-cell 6061 Al foam) and Wang et al. [42] up to 113 m s^{-1}. No strain rate sensitivity of brittle foams made of Al alloys was determined at relatively low velocities in refs. [7] and [37]. The deformation in these brittle foams proceeded with progressive cell wall collapse, including cell wall buckling and cell wall tearing modes. The quasi-static collapse in ductile foams started at the weakest band of cells, usually in the interior of the samples, while the cell collapse started at the impact end and sequentially propagated to the uncrushed sections in a planner manner above the critical velocities [17, 39]. Agreements between the calculated and experimentally

determined critical velocities (41-108 m s^{-1}) were found for Hydro/Cymat foams [17, 39]. Somewhat similar critical velocity range was determined for an open-cell 6061 Al foam; the specimens impacted at 60 m s^{-1} or above showed shock deformation, while the specimens impacted below 40 m s^{-1} showed very similar crushing mode with the specimens tested at quasi-static velocity [16]. As with aluminum honeycombs, three deformation modes were reported for Al foams [42]: the sample's back and front surface stresses were equal corresponding to the homogeneous mode at 16 m s^{-1}, the front surface stress was higher than that of the back surface showing the inertial effect or shock deformation mode at 113 m s^{-1} and the transition mode at the intermediate velocity of 63 m s^{-1}.

1.4. The Motivation for Present Thesis

There have been many studies on the impact behavior of Al foams [2, 7, 24, 25, 38, 39] and honeycombs [18, 31]. The dynamic deformation and shock stress formation in cellular structures have also been extensively investigated using FE analysis. Few examples to these studies include in-plane crushing of a hierarchical honeycomb [43], aluminum closed-cell foams [20], single- and double-layer aluminum corrugated core [44] and aluminum open cell foams [28]. But, it is found, through an extensive inspection of the current literature, that the studies of the effect of material model parameters on the dynamic deformation of cellular structures are few. The only numerical study performed was on the out-plane plateau stresses of a honeycomb structure up to 180 m s^{-1} using a strain rate hardening Al material model with various strain rate hardening parameters [33]. It was shown in the same study that the stress increase due to the strain rate sensitivity of cell wall material was only effective until about very low velocities (~10 m s^{-1}), while inertia including micro-inertia was dominant at relatively high velocities. It seems that there exists a lack of the knowledge of the effects of strain hardening and strain rate hardening on the dynamic deformation particularly shock deformation of cellular structures.

The aim of the present study was to determine numerically the effect of the material model on the crushing behavior of a layered 1050 H14 aluminum corrugated sandwich structure as function of velocity. Since the crushing strength of Al foams shows high variations for the same density [7], a multilayer structure with a homogenous cellular

structure was selected. The investigated multi-layer sandwich core was made of multilayer corrugated layers (fins) and was previously shown to exhibit repeatable load-displacement responses to mechanical forces [26, 45, 46]. Three different material models were selected for modelling purpose: elastic-perfectly plastic, elastic-plastic strain hardening, elastic-plastic strain and strain rate hardening. The homogeneous layers of a multi-layered structure with 3D full models allowed to monitor the stress, strain and velocity histories of each layer during the course of deformation. Three-dimensional finite element models were developed in the explicit finite element code of LS-DYNA. The quasi-static compression model was at 0.0048 m s^{-1} and the direct impact models were at 20, 60, 150 and 250 m s^{-1}.

There exist various sizes of imperfections or irregularities in cellular structures, which reduce the elastic modulus, bending and buckling stresses. Previously several numerical imperfections were implemented to account the imperfection effect on the crushing behavior of cellular structures. These include the distortion in the mesh, node shaking, pre-buckling of cell walls, modelling the actual size of cell wall [47], implementing random mechanical properties [48] and deflection in truss strut [49]. In present study, the multilayer corrugated structure was modelled using geometrically imperfect layers. These imperfect layers were inserted into the geometry to represent localized imperfections.

In the thesis, the quasi-static and dynamic modelling methodologies are given in Chapter 2, the quasi-static and dynamic modelling results in Chapter 3, the discussion of the results in Chapter 4 and finally the conclusions in Chapter 5.

CHAPTER 2

MODELLING

2.1. Modelling Methodology

The initial modelling efforts were on the determination of the representative models for the quasi-static compression stress-strain behavior of the corrugated multi-layered sandwich core structure. Therefore, various imperfect fin geometrical models were implemented along with the perfect unit fin model. Once the representative numerical model geometry was determined, the direct impact models were then implemented in order to determine the effect of strain and strain rate hardening on the stress-strain behavior of the corrugated structure.

The investigated multi-layered sandwich core structure was made of 1050 H14 Al trapezoidal zig-zag corrugated layers (fins) as seen in Figure 2.1(a). The sandwich structure was constructed using 15 zig-zag fin layers. The height, width, length and thickness of a fin are sequentially 3.20, 1.6, 2.4 and 0.170 mm (Figure 2.1(b)). The corrugated Al fin layers were produced by a local factory using a sheet-forming process which deformed the sheet metal by the help of a press into a regular trapezoidal shape in few steps. Later, the fin layers were assembled by a brazing process. The brazed multi-layered corrugated sandwich panel shown in Figure 2.1(a) is 500x500x50 mm in size and assembled in 0/90 fin layer configuration. The face sheets, 1 mm thick 1050 H14 sheet, prevent the mechanical damaging of the layers in brazing and subsequent machining operations. Cylindrical compression test sample 19.40 mm and 40 mm in diameter were extracted from the sandwich plate by means of an electro-discharge machine and the face sheets were removed later again using the electro-discharge machine . The test sample had a density of 326 kg m^{-3} without face sheets. The test sample contained typical fin wall imperfections induced during the brazing and cutting processes. During sample cutting, the fin walls at the outer surface were significantly bent. These imperfections are likely to alter the location of the initial layer collapse and crushing stress. Second, the fin walls were noted to be thicker at the fin contact points which were attributed to the filler

accumulation at these sites. The thicker contact points may affect the densification strain and stress values.

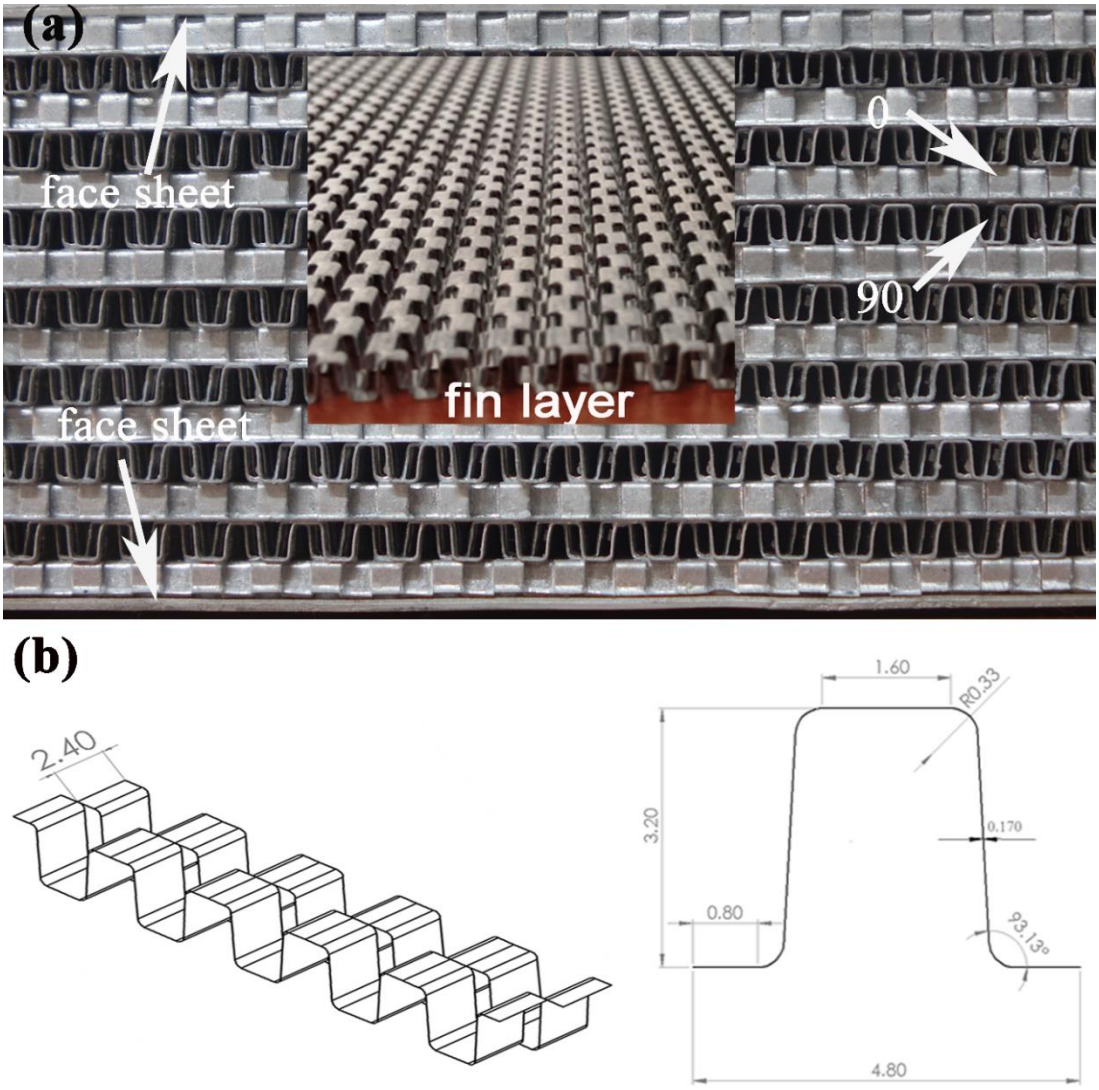

Figure 2.1. (a) The multi-layered sandwich plate cross-section and fin layer and (b) fin geometrical sizes

The as-received sandwich plate contained typical fin wall imperfections induced during brazing. The fin walls were slightly bent after brazing. In addition, the fin walls at the outer surface of the cylindrical samples were significantly bent after cutting, while interior fin walls were not affected. The surface bent fin walls were simulated using double-imperfect fin in the layers. The 3D corrugated test sample models were constructed using three different fin geometries. These are the perfect, imperfect and double imperfect fins as shown in Figures 2.2(a-c), respectively. The perfect, imperfect and double imperfect fin models had the same geometrical properties with the test sample

fins, except the thickness of the fin walls increased to 0.187 mm in order to account the used filler material weight in the brazing process (7 wt%- corresponding to 0.018 mm thickness increase). In the imperfect and double imperfect fin models, a bent type of imperfection, 1.62 mm in radius, is introduced to the one and two legs of the fins (Figure 2.2 (b) and (c)).

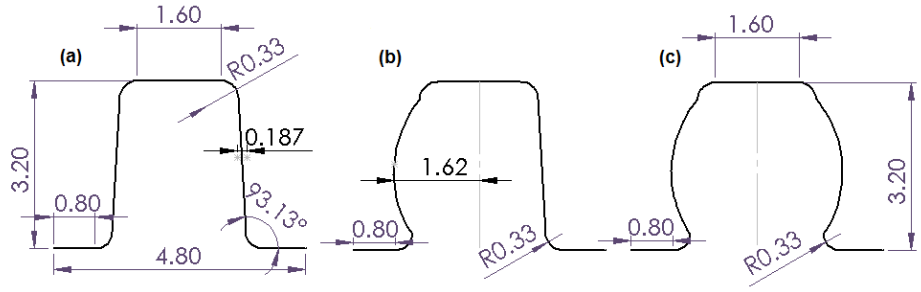

Figure 2.2. (a) perfect, (b) imperfect and (c) double imperfect unit fin geometries

The quasi-static tests models were created using 6 different test sample models as shown in Figures 2.3(a-f). These test sample models are coded as perfect model I, perfect model II, one-layer imperfect, two-layer imperfect, one-layer double imperfect and two-layer double imperfect models (Figures 2.3(a-f)). In the perfect model I, all layers were constructed using perfect unit fin geometry (Figure 2.3(a)). In perfect model II, all layers were constructed using imperfect fins (Figure 2.3(b)). In one-layer imperfect model, only tenth-layer was constructed using the imperfect fins and the others were made of perfect fins (Figure 2.3(c)). In two-layer imperfect model tenth and second layers were made of imperfect fins and others were made of perfect fins (Figure 2.3(d)). In one-layer double imperfect model, the tenth layer was constructed using double imperfect fins and the others were made of imperfect fins (Figure 2.3(e)). In two-layer double imperfect model, tenth and second layers were made of double imperfect fins and the rest were made of imperfect fins (Figure 2.3(f)).

The models were created in Hyper Mesh 13.0 software. The zig-zag shape of the structure was generated using the method of duplication of meshed unit cell. The finite element models were then imported to LS-Dyna Pre-post Software as '.k' file and boundary conditions, initial conditions, material properties, contact types and areas, termination time and shell thickness were defined in the LS-Dyna Pre-post. All analyses were run using non-linear explicit solver in LS-Dyna software. The results were processed with preprocessor and finally the simulation and the test results were compared

to validate the test models. The perfect model I contained 125906 shell elements. The perfect model II and one-layer imperfect, two-layer imperfect, one-layer double imperfect, two-layer double imperfect models contained 150871, 132335, 133668, 152512 and 154153 shell elements, respectively.

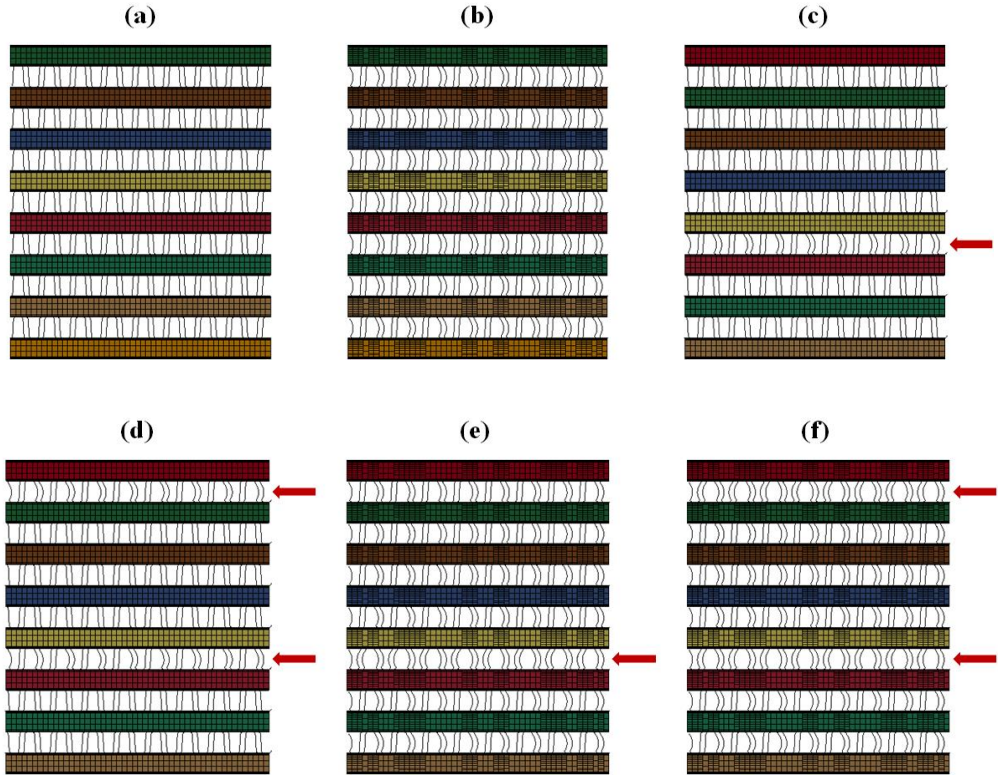

Figure 2.3. (a) perfect model I (b) perfect model II (c) one-layer imperfect model (d) two-layer imperfect model (e) one-layer double imperfect model (f) two-layer double imperfect model

2.2. Quasi-static Model

The used quasi-static compression test model is shown in Figure 2.4. The crossheads of Shimadzu testing machine were modelled with MAT_RIGID (Material type 20). The modulus of elasticity (E) of the crossheads steel was taken 210 GPa and the Poisson's ratio (v) is 0.3. The bottom crosshead was constructed using 19200 solid elements and constrained in all directions (fixed in x, y-, z-displacement and rotation). Top crosshead was modelled again using 19200 solid elements and moved only through the axial-direction with a velocity same as the compression test velocity, 4.8×10^{-3} m s^{-1}. The specimen was modelled with MAT_SIMPLIFIED_JOHNSON_COOK material model.

$$\sigma_y = [A + B\varepsilon_P^n][1 + cIn\dot{\varepsilon}_P^*][1 - T_H^m] \quad (2.1)$$

where σ_y is the equivalent stress, A and B are the constants, ε_P is the equivalent plastic strain, n is the strain hardening parameter, c is the strain rate sensitivity parameter, $\dot{\varepsilon}_P^*$ is the strain rate ratio calculated as $\frac{\dot{\varepsilon_p}}{\dot{\varepsilon_0}}$, where $\dot{\varepsilon_P}$ is the equivalent plastic strain rate, $\dot{\varepsilon_0}$ is the reference equivalent plastic strain rate, T_H is the normalized temperature expressed as $T = \frac{T-T_r}{T_m-T_r}$ where T, T_r and T_m are the temperature, room temperature and melting temperature, respectively. However, the effect of temperature is not taken into consideration in this simplified card. The material model parameters of 1050 H14 Al sample were determined previously as A=102 MPa, B=97.25 Mpa, n=0.18 and $\dot{\varepsilon_0}=10^{-3}$ s^{-1} [45].

Various cards were used for defining the initial and boundary conditions. BOUNDARY_PRESCRIBED_MOTION_RIGID card was used to give constant z-direction velocity to the top crosshead. Total time of the quasi-static simulation was defined with CONTROL_TERMINATION card. Since the total CPU time for the quasi-static test solutions are relatively long, the mass scaling was applied in the quasi static simulations by defining a positive time step value in CONTROL_TIMESTEP card. The mass was added or removed from the elements. In order to determine the mass scaling factor, the simulation was initially run without mass scaling and the determined time step without mass scaling was multiplied by 10, 100 and 1000. It was found numerically that the kinetic energy change was substantially lower than the internal energy change when the mass scaling factor was 1000. Termination time was taken as 10000 milliseconds. The mass scaling method was put into model to reduce the calculation time by using CONTROL_TIMESTEP card (Time step size for mass scaled solutions, DT2MS is 0.0198). The contacts between steel crossheads and specimen were determined with AUTOMATIC_SURFACE_TO_SURFACE. The static and dynamic coefficients of frictions were defined as constant 0.3 and constant 0.2, respectively. CONTACT_ERODING_SINGLE_SURFACE card was used to define the contacts between each layer of the specimen.

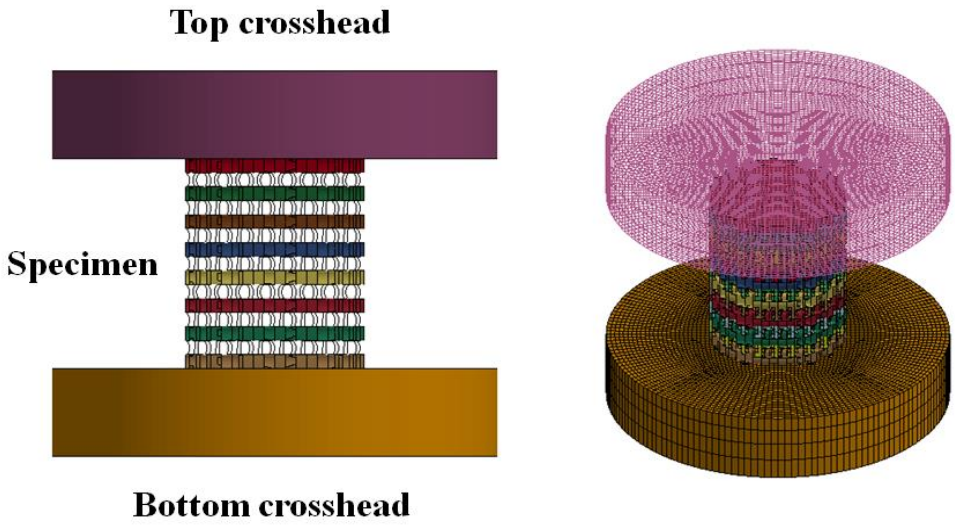

Figure 2.4. Front and isometric views of the quasi-static numeric model

2.3. Dynamic Model

In the SHPB direct impact tests, the test specimen is placed in front of incident bar and striker bar with an initial velocity impinge the specimen, deforming it until about large strains (Figure 2.5(a)). The test specimen in the experiments was attached to the center of the incident bar using lubricant which was strong enough to hold the specimen in front of the incident bar (Figure 2.5(b)). During the test, the stress on the incident bar was measured using two full-bridge strain-gage circuits; one was 300 mm and the other was 1110 mm away from impact end. The former gage is coded as the front strain gage and the latter as the back strain gage (Figure 2.5(a)). The striker bar velocity was measured just before the impact of the striker bar to the test sample using two laser diodes placed at the exist of the gas gun barrel (Figure 2.5(b)). The velocity of the striker bar was altered by changing the SHPB gas gun pressure. The striker bar had the same diameter, 19.40 mm, with the incident bar.

The full model direct impact test model and the specimen bar interfaces are shown in Figure 2.6. The inconel 718 incident bar, inconel 718 and aluminum striker bar were modeled using 15 mm size elements. The Inconel bar with a length of 20 cm was used to model the direct impact tests at 20 m s^{-1}, while 60 and 150 m s^{-1} models were modelled using 15 cm long aluminum striker bar. The numbers of elements of the incident and striker bars were 28980 and 4800, respectively. To provide compatibility between the numerical model and test conditions, the striker bar moves only z-direction. The transitional and rotational movements were constrained in other directions. The inconel

and aluminum bars were modelled using MAT_ELASTIC material model (Material type 01). The density, elastic modulus and Poisson's ratio of the inconel were taken as 7850 kg m^{-2}, 207 Gpa, 0.33, respectively. The density, elastic modulus and Poisson's ratio of aluminum were taken as 2810 kg m^{-3}, 71.70 Gpa and 0.33, respectively.

The contacts between striker bar and incident bar were defined by the AUTOMATIC_SURFACE_TO_SURFACE contact algorithm. The contacts between the layers of specimen were defined by the AUTOMATIC_SINGLE_SURFACE algorithm. The static and dynamic friction coefficients at the bar contacts were taken 0.2 and 0.1, respectively and the dynamic and static friction coefficients at the layer contacts were taken 0.3 and 0.2, respectively. The data were taken in striker and incident contact cards. Total time of the dynamic simulation was defined by the CONTROL_TERMINATION card. Termination time was taken as 3 milliseconds. The initial velocity was defined by the INITIAL_VELOCITY_GENERATION card.

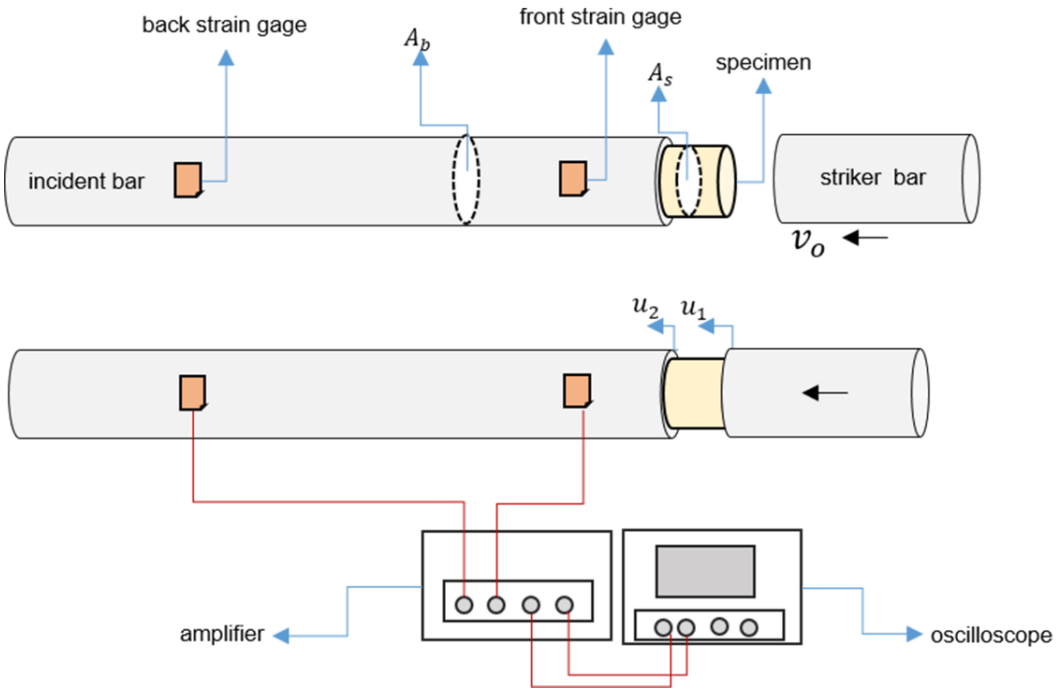

(a)

Figure 2.5. (a) The schematic drawing of direct impact test and (b) the picture of experimental direct impact set-up

(cont. on next page)

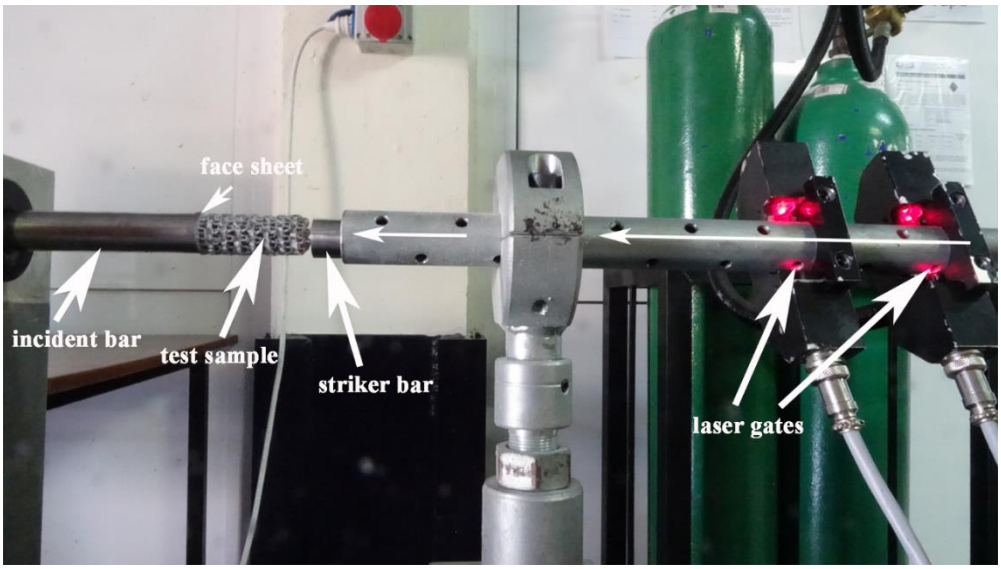

(b)

Figure 2.5. (cont.)

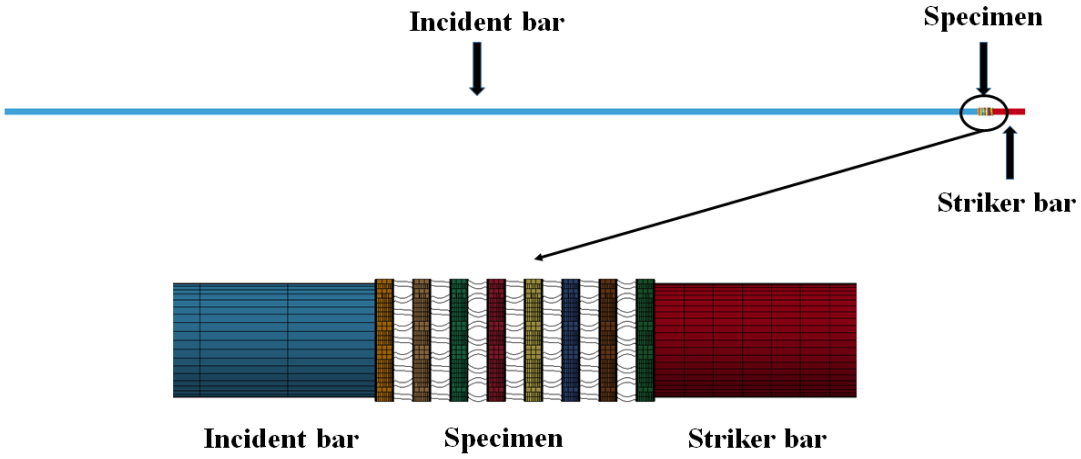

Figure 2.6. The SHPB test model and interfaces between bars and specimen

In the direct impact test models, three different material flow stress models were selected and implemented. These were respectively (1) the perfect plastic with no strain rate hardening material model (A=102 Mpa, B=0 Mpa, n=0, c=0 and m=0), (2) the strain hardening with no strain rate hardening material model (A=102 Mpa, B=97.25 Mpa, n=0.18, c=0 and m=0), and (3) the strain hardening with strain rate hardening material model (A=102 Mpa, B=97.25 Mpa, n=0.18, c=0.02 and m=0). The strain rate dependency constant "c" was defined as 0.02 for aluminum alloys based on Meyers' book [50].

Material models were coded as material model I, material model II and lastly material model III respectively. And the stress-strain behaviors of the models are shown in Figure 2.7. Material model II is used to determine the effect of strain hardening and material model III used to determine the effect of strain rate hardening.

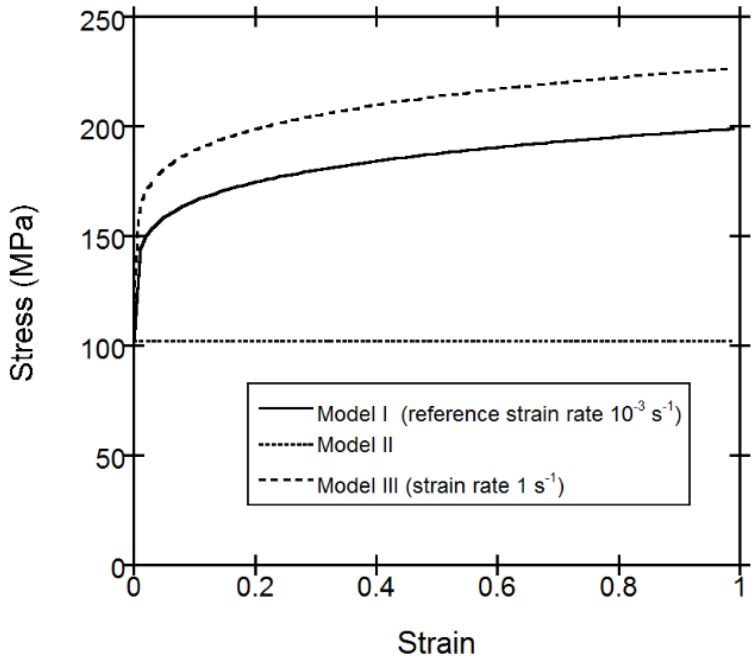

Figure 2.7. The stress-strain curves of the material model I, model II and model III

CHAPTER 3

RESULTS

3.1. Quasi-static Tests and Model Selection Studies

The quasi-static ($4.8x10^{-3}$ m s^{-1}) stress-strain and mean stress-strain curves of the tested two corrugated samples are shown in Figure 3.1. The quasi-static tests were performed by Sarıkaya in the previous study [51]. The quasi-static stress-strain behavior of the corrugated sample as seen in Figure 3.1 clearly indicates the characteristics of cellular metal's stress-strain behavior. Initially the sample deforms elastically until about an initial peak/crushing stress; thereafter, the strain localization occurs in the form of development of a deformation/crush band with the crushing of a single fin layer or two fin layers. Noted from the deformation micrographs, the deformation band(s) forms progressively but non-sequentially (random) as the strain increases until about a densification strain after which the stress values increase sharply. The region between the initial peak stress and the densification strain as seen in Figure 3.1 is called the plateau region. The plateau region is characterized by a constant or oscillating stress known as the plateau stress. As is shown in Figure 3.1, the initial peak stresses of the quasi-statically tested samples vary between 1.38 and 1.58 Mpa with an average of 1.45 Mpa. The densification strain was determined by the intercept method. A tangent line is drawn to the densification part of stress-strain curve and the intercept of this line with mean crushing stress was taken as the densification strain. The experimental densification strain by this method is determined 0.67 as shown in Figure 3.1.

The effect of fin wall thickness on the quasi-static velocity (4.8x10-3 m s^{-1}) stress-strain behavior of the corrugated core was initially investigated by modeling the perfect model I of material model II (strain hardening with no strain rate hardening). From these models, an optimum fin wall thickness representing the test was determined. Thereafter, the effect of other models on the stress-strain behavior was investigated using the determined fin wall thickness. The effect of fin wall thickness was investigated using six different thicknesses: 0.100, 0.135, 0.145, 0.170, 0.187 and 0.200 mm. The quasi-static stress-strain curves of the perfect model I at the investigated thicknesses are shown

together with the test's stress-strain curve in Figures 3.2(a) and (b) for 0.100, 0.135 and 0.170 and 0.170, 0.187 and 0.200 mm, respectively. As seen in the same figures, as fin wall thickness increases, both the initial peak stress and plateau stress increase. Increasing fin wall thickness also increases the peak and valley stresses. As is seen in Figure 3.2(b), when fin wall thickness increases to 0.170-0.200 mm, the perfect model valley stresses become almost equal to those of the test, while the model peak stresses are higher than those of the test. The modelling is therefore continued with a fin wall thickness of 0.187 mm. This pre-determined fin wall thickness is noted to agree well with the fin wall thickness of the corrugated core if 7wt% of filler material used as binder in brazing is equally distributed to fin walls.

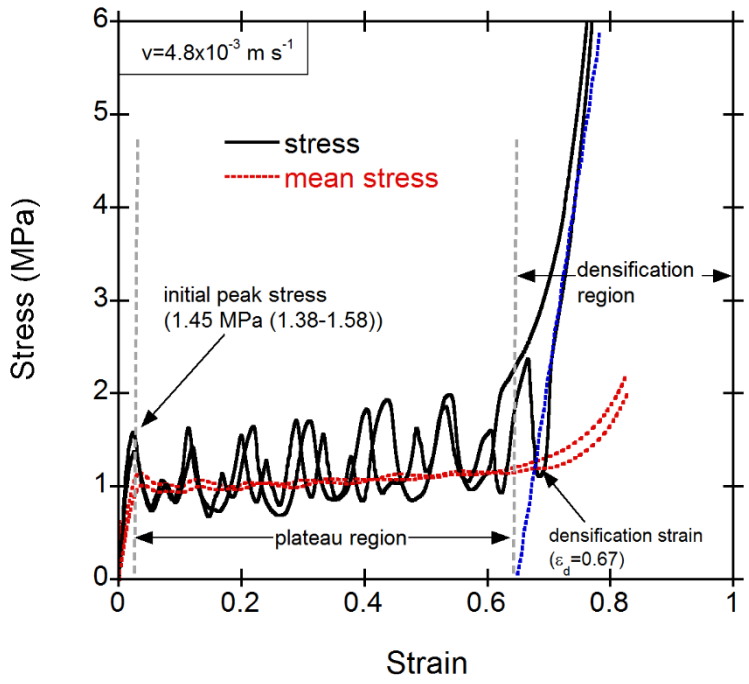

Figure 3.1. The quasi-static ($4.8x10^{-3}$ m s^{-1}) stress-strain and mean stress-strain curves of the corrugated core

The stress-strain curves of the perfect model I, one-layer and two-layer imperfect models of material model II with 0.187 mm fin wall thickness are shown in Figure 3.3. The inclusion of imperfect layer(s) is noted in the same figure to decrease, as compared with the perfect model, the initial peak stress without significantly affecting the plateau stress and densification strain. The imperfect layer however changes the deformation sequence of layers and this change will be elaborated below.

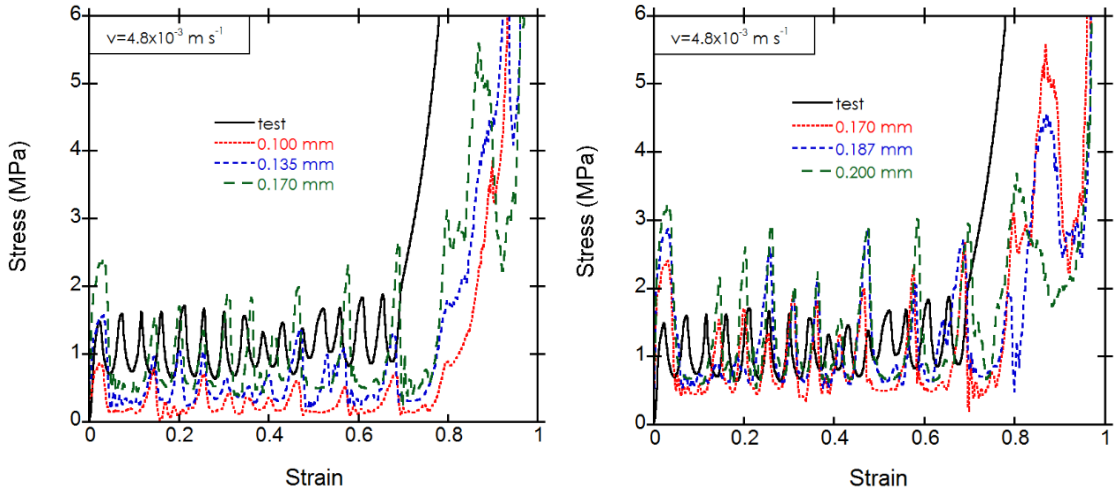

(a) (b)

Figure 3.2 The quasi-static stress-strain curves of the perfect model I at (a) 0.100, 0.135, 0.145 and 0.170 and (b) 0.170, 0.187 and 0.200 mm fin wall thickness

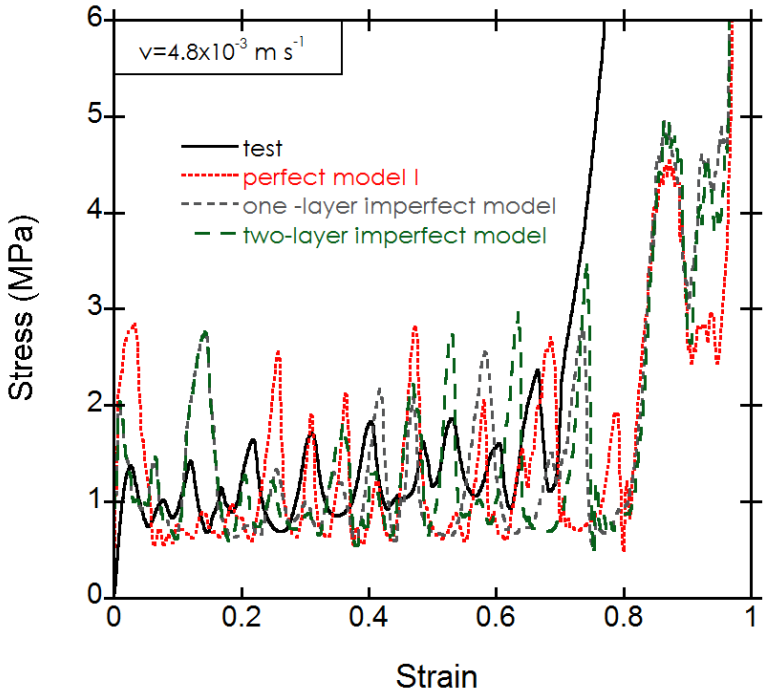

Figure 3.3 The quasi-static stress-strain curves of the perfect model I, one-layer imperfect and two-layer imperfect models with 0.187 mm fin wall thickness

The deformation pictures of the test, perfect model I, one-layer imperfect model and two-layer imperfect model of material model II with 0.187 mm fin wall thickness at 0, 0.2, 0.4, 0.6 and 0.8 strain are shown sequentially in Figures 3.4(a-d). The layer crushing initiates at the bottom sections of the test sample as seen in Figure 3.4(a) at the strain of 0.2. Then, the layer crushing continues at the upper layers as the strain increases.

The layer crushing causes shearing of the layers, which causes the bending of the test sample as seen in Figure 3.4(a) at 0.4 and 0.6 strain. It is also noted that the midsection layers crush at a later stage of the deformation. The layer crushing starts at the bottom and top sections of the perfect model I as seen in Figure 3.4(b). As similar with the test sample, the numerical midsection layers crush at a later stage. The extent of specimen bending is significantly declined in the perfect model I. In the one- and two-layer imperfect models, the layer crushing however initiates at the 2nd and 10th layer (imperfect layers) as seen in Figures 3.4(c) and (d). Later, the layer crushing switches to the top and bottom layers and then switches to the midsection layers. The specimen bending is clearly seen in Figures 3.4(c) and (d). The specimen bending starts at about the strain of 0.4, almost the same as the test sample. The test deformation sequence and final deformed shape of the test sample are therefore concluded to be well approached by the imperfect models.

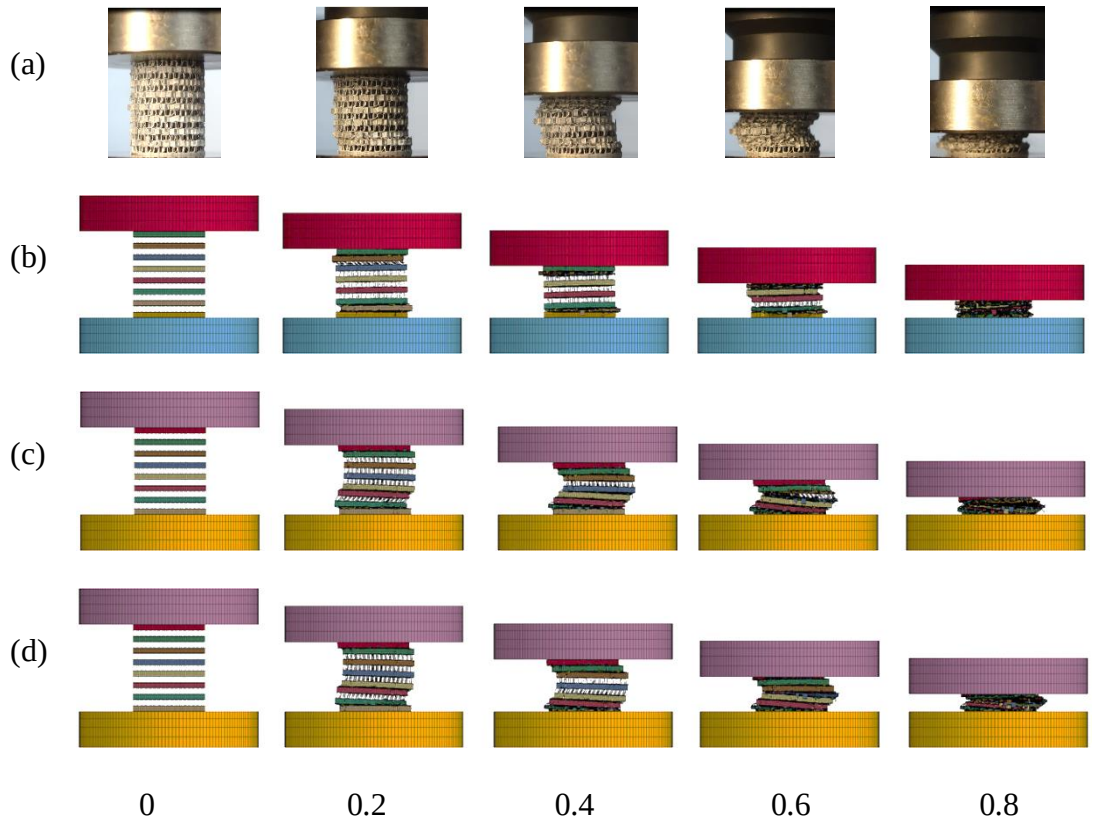

Figure 3.4. The quasi-static deformation pictures of (a) test, (b) perfect model I (c), one-layer imperfect and (d) two-layer imperfect models with 0.187 mm thickness at 0, 0.2, 0.4, 0.6 and 0.8 strain (numbers below show strain)

The stress-strain curves of the test, perfect model II and two-layer double imperfect model of material model II with 0.187 mm fin wall thicknesses are shown in Figure 3.5. The initial crushing stress, as compared with the perfect model I, further decreases as seen in Figure 3.5 with the implementation of the perfect model II and double imperfect model. It is noted that the peak and valley stresses and the densification strain of the test sample are well predicted by the perfect model II and the two-layer double imperfect model. The one-layer double imperfect model, although not shown here, also resulted in similar stress-strain behavior with the two-layer double imperfect model.

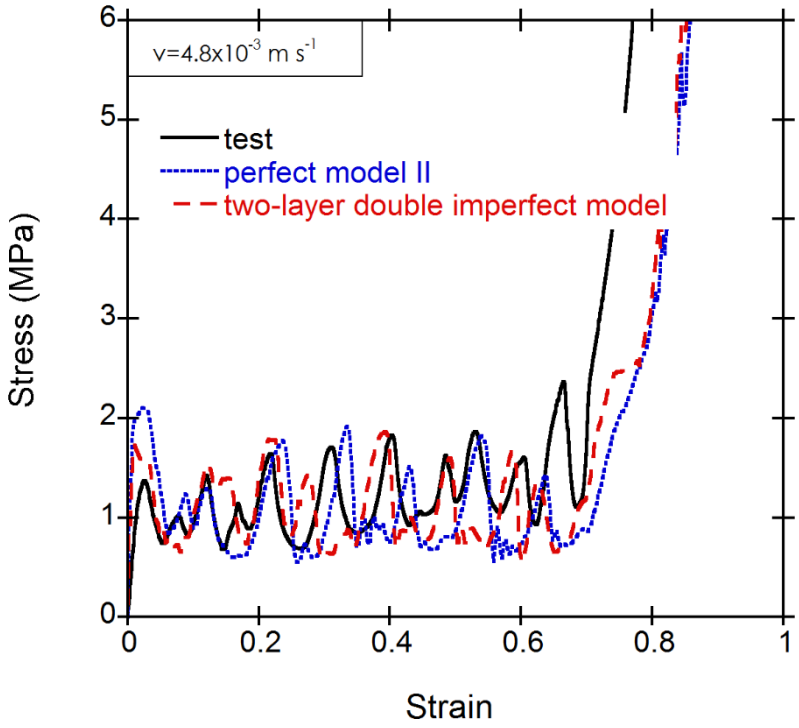

Figure 3.5. The quasi-static stress-strain curves of the test and perfect model II, two-layer double imperfect model at 0.187 mm thickness

The deformation pictures of the perfect model II, one-layer double imperfect and two-layer double imperfect models of material model II with 0.187 mm fin wall thickness at 0, 0.2, 0.4, 0.6 and 0.8 strain are shown in Figures 3.6(a-c), respectively. The initial layer crushing in the perfect model II starts, as similar with the perfect model I, at the bottom and top section layers. And similarly, the midsection layers crush at later stages (Figure 3.6(a)). In the one-layer double imperfect model, the layer crushing starts at the 10^{th} layer and then progresses with the crushing of the layers at the top and bottom sections. The layer crushing sequence in this model is as following: 10, 2, 14, 3, 13-15, 5, 1, 11, 4-6, 8, 9-12 and 7.

The layer crushing in the two-layer double imperfect model starts at the imperfect layers and the layer crushing sequence in this model is 10 -8, 2-12, 6, 4, 14, 13, 5, 7-11, 9, 1 -15 and 3. The deformation mode is seen to be very similar to that the test (Figure 3.6(c)); therefore, the further modeling was continued with the two-layer double imperfect model.

The effect of fin wall thickness on the crushing behavior of the two-layer double imperfect model of material model II is shown in Figure 3.7. As the fin wall thickness increases both the initial peak stress and plateau stress increase, while the densification strain decreases. It is also noted that the deformation modes of the two-layer double imperfect models of material model II with 0.135, 175 and 187 mm fin wall thicknesses are very similar as depicted in Figures 3.8(a-c).

Mesh sensitivity analysis of the two-layer double imperfect model of material model II was performed using 0.4 and 0.2 mm mesh sizes. The use of 0.4 mm mesh size resulted in similar stress-strain behavior with 0.8 mm mesh size, while 0.2 mm mesh size model resulted in relatively long termination time. Therefore, the models were continued with 0.8 mm mesh size.

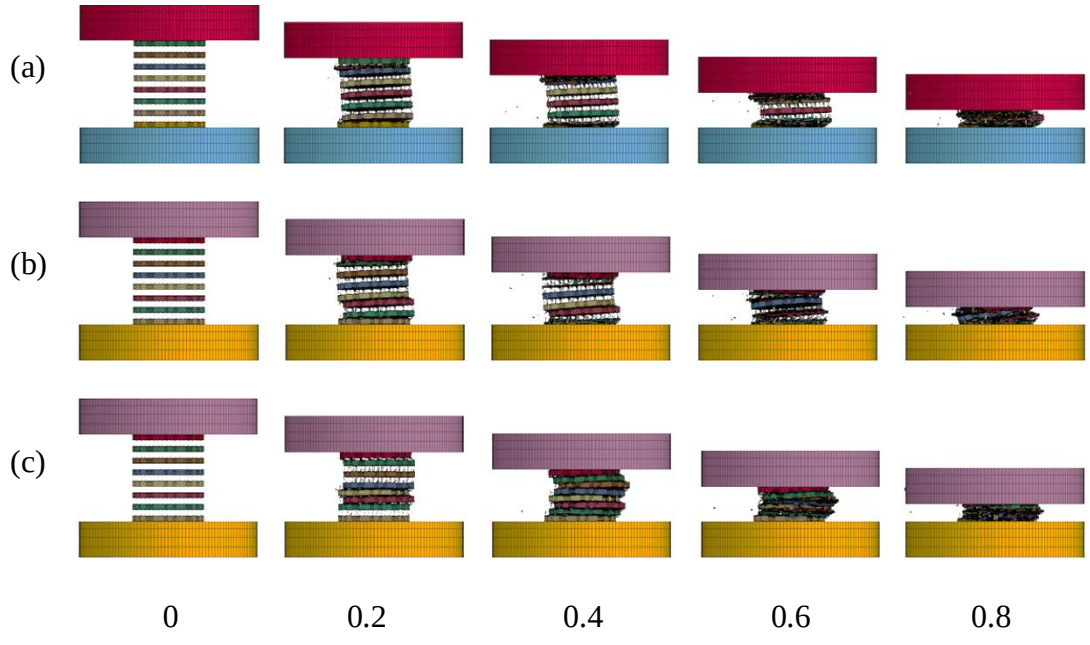

Figure 3.6. The quasi-static deformation pictures of (a) the perfect model II, (b) one-layer double imperfect model and (c) the two-layer double imperfect model with 0.187 mm fin wall thickness at 0, 0.2, 0.4, 0.6 and 0.8 strain

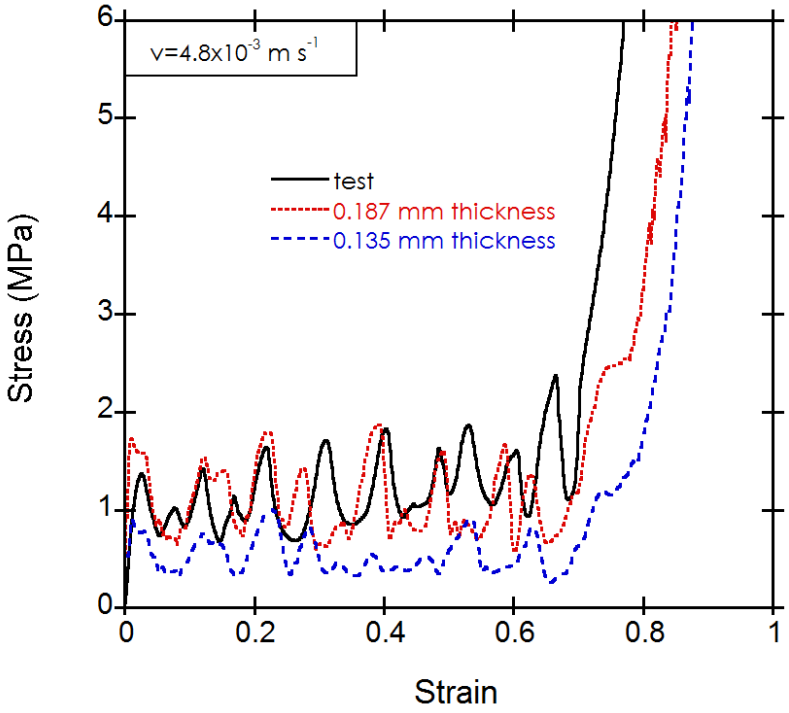

Figure 3.7. The quasi-static stress strain curves of the test and two-layer double imperfect model with 0.135 and 0.187 mm fin wall thicknesses

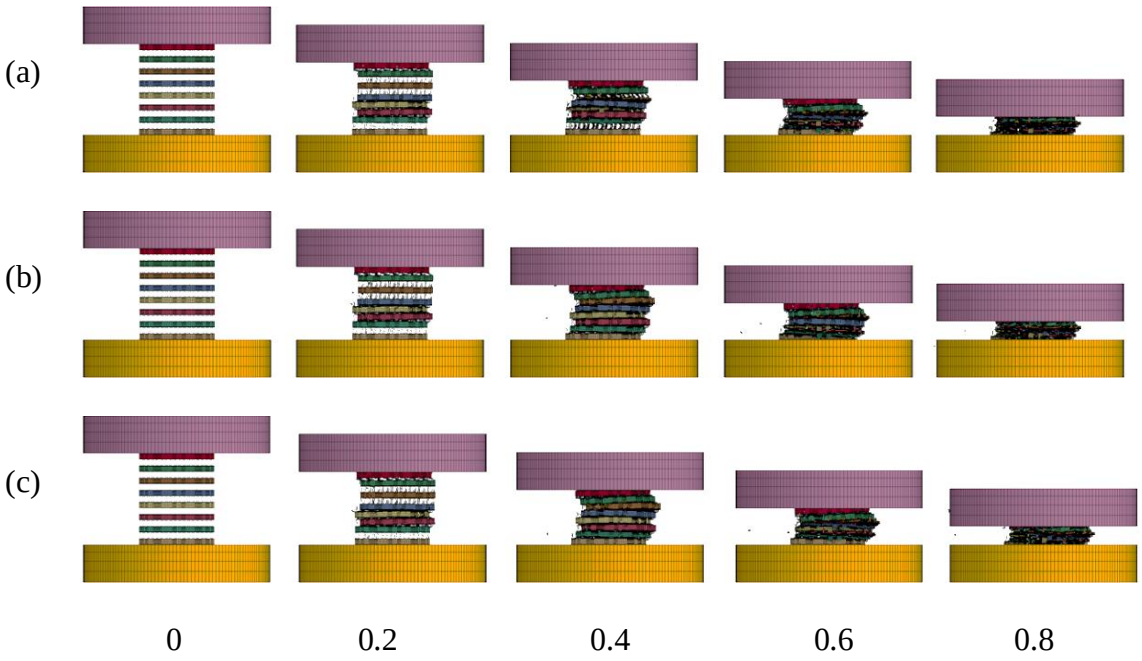

Figure 3.8. The quasi-static deformation pictures of the two-layer double imperfect models with (a) 0.135, (b) 0.170 and (c) 0.187 mm fin wall thicknesses

3.2. Quasi-static Models

The quasi-static stress strain curves of the two-layer double imperfect model of material model I (perfect plastic with no strain rate hardening), model II (strain hardening with no strain rate hardening) and model III (strain hardening with strain rate hardening) are shown in Figure 3.9. It is noted in the same figure the material model II and III exhibit almost the same stresses as the strain rate is relatively low, while the material model I results in relatively low initial peak stress and plateau stress as the strain hardening. The increased stresses of the material model II and III as compared with the material model I are due to the strain hardening. The strain hardening also affects the densification strain; it decreases the densification strain as seen in Figure 3.9. The initial peak stresses are 1.25 MPa for the material model I and 1.73 MPa for the material model II and III. The quasi-static deformation pictures of the two-layer double imperfect model of the material model I, II and III are shown sequentially in Figures 3.10(a-c). Although the deformation profiles of material model II and III are very much similar to each other and also to the test, the deformation mode of the material model I is different. The layers in the material model I are inclined to the loading axis at the beginning of the crushing, leading to reduction of the crushing stresses until densification strain (Figure 3.10(a)).

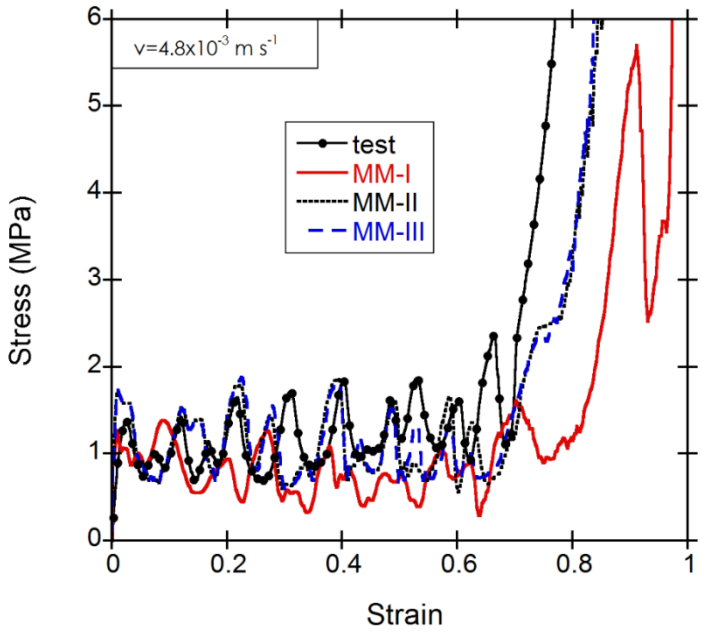

Figure 3.9. The quasi-static stress strain curves of the two-layer double imperfect model of the material model I, II and III

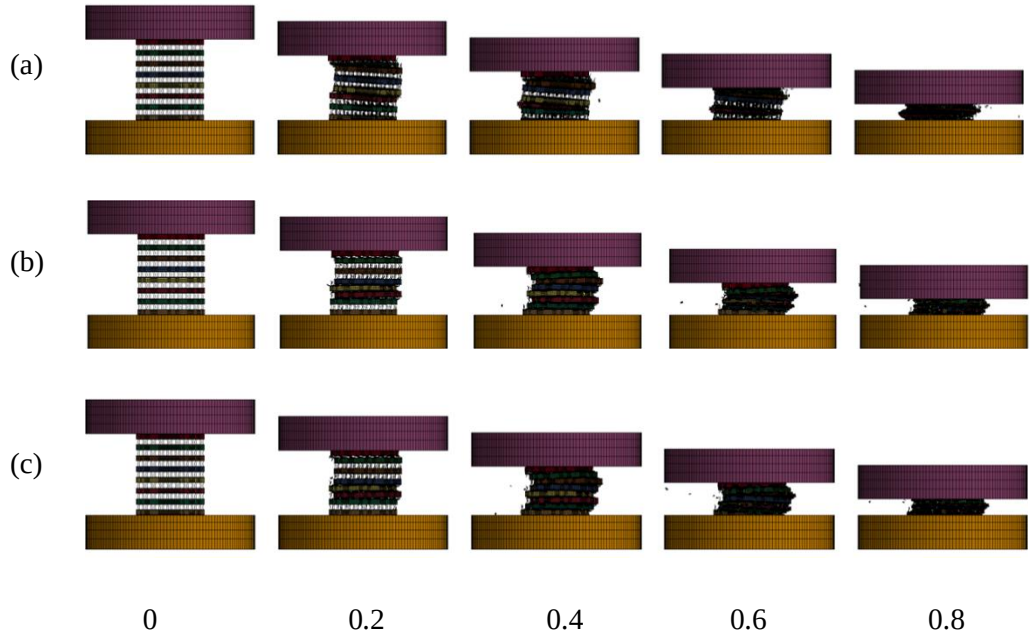

Figure 3.10. The quasi-static deformation pictures of the two-layer double imperfect model of (a) the material model I, (b) II and (c) III

3.3. Dynamic Models

The distal end and the impact end stress-time curves of the material model I, II and III at 20 m s^{-1} are shown in Figures 3.11(a) and (b), respectively. As is seen in the same figures, the material model III gives the highest and the material model I gives the lowest initial peak stresses. The distal end and impact end peak stresses are 1.61 MPa and 1.91 MPa, 2.05 and 2.3 MPa and 2.44 and 2.75 MPa for the material model I, II and III, respectively. The differences between the distal end and impact end peak stresses are 0.3 MPa, 0.25 MPa and 0.31 MPa for the material model I, II and III, respectively.

The initial peak stresses increase over those of the quasi-static models (the initial peak stresses are 1.25 MPa and 1.73 MPa for the material model I, material model II and material model III) at this velocity. The effect of deformation velocity is also seen in Figures 3.11(a) and (b); the strain rate hardening material model III shows a higher initial peak stress than the strain hardening material model II and also perfect plastic with no strain rate hardening material model I.

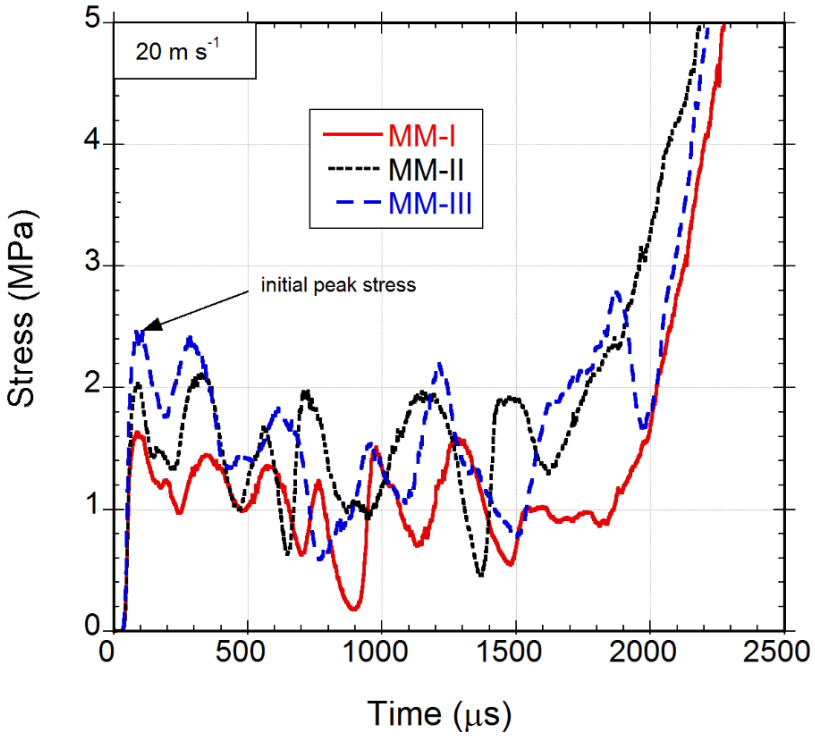

(a)

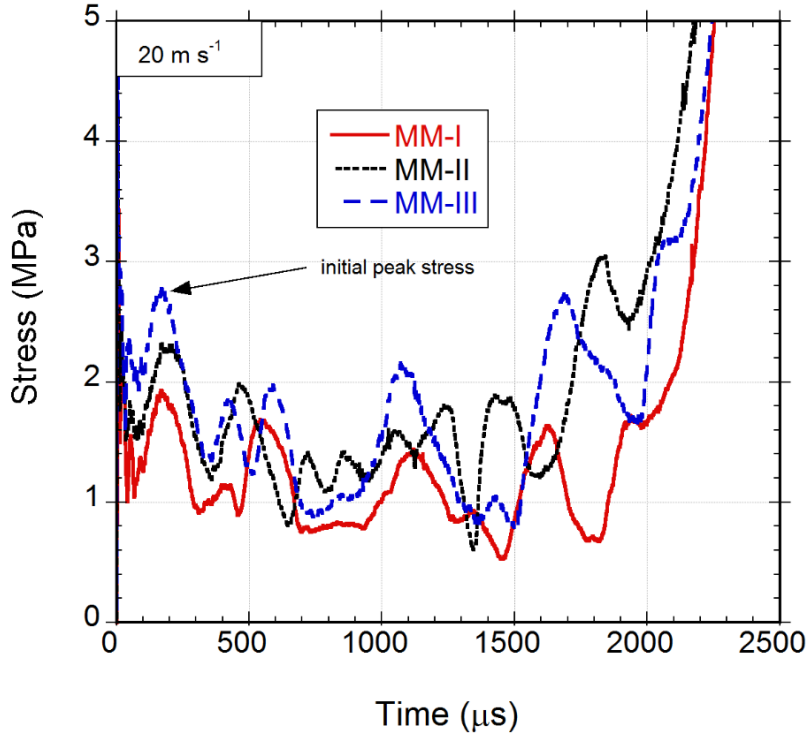

(b)

Figure 3.11. The stress-time curves of the material model I, II and III at 20 m s^{-1}: (a) distal end and (b) impact end

Figure 3.12(a-c) shows the distal end and impact end stress-time profiles of the material model I, II and III, respectively. Except the initial peak stress, the distal and impact end stresses are almost equal to each other for the investigated three material models at 20 m s^{-1}.

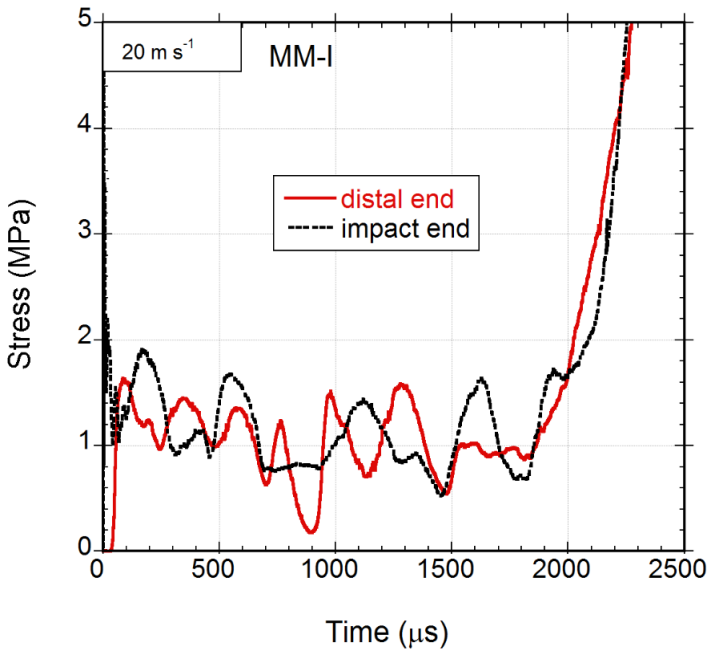

(a)

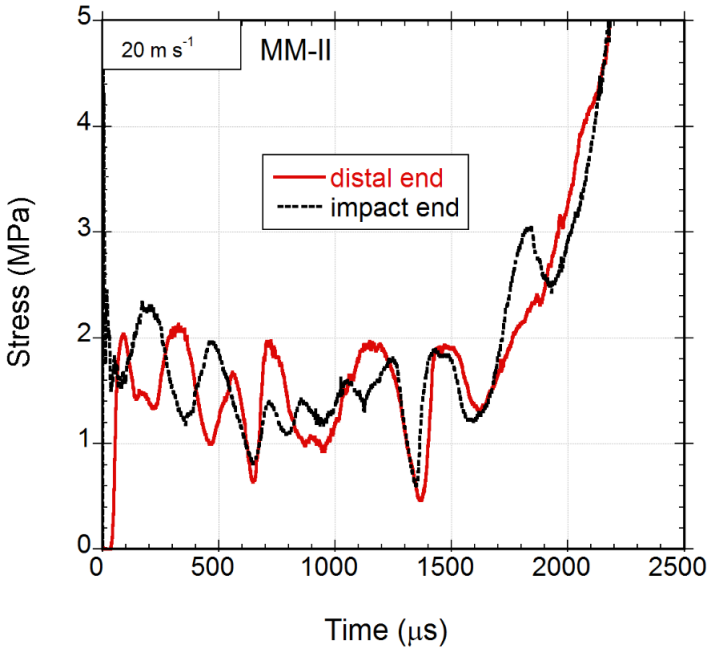

(b)

Figure 3.12. The distal end and impact end stress-time curves of the material (a) model I, (b) II and (c) III at 20 m s^{-1}

(cont. on next page)

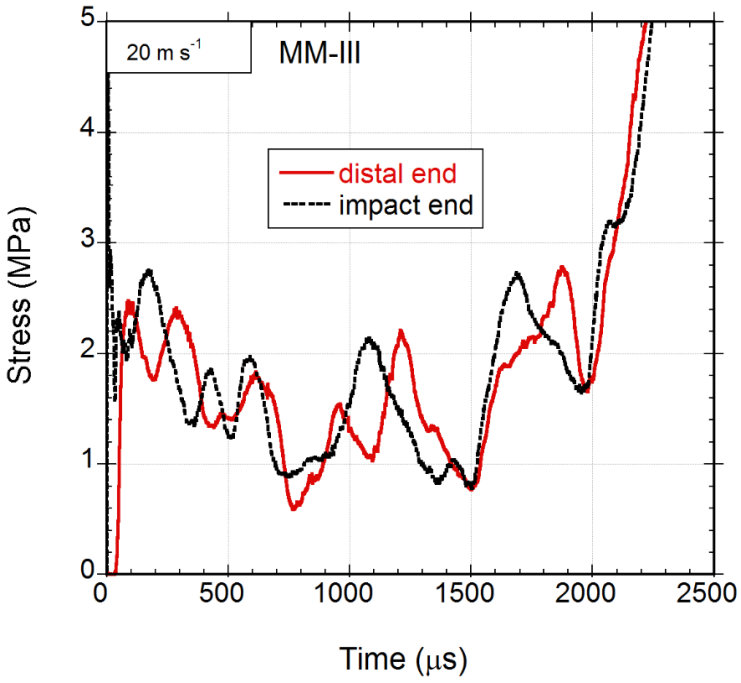

(c)

Figure 3.12 (cont.)

The layer crushing at 20 m s^{-1} for the three material models initiates near the impact end, but the deformation bands formed are although progressive form the impact to the distal end not sequential as seen in Figures 3.13(a-c).

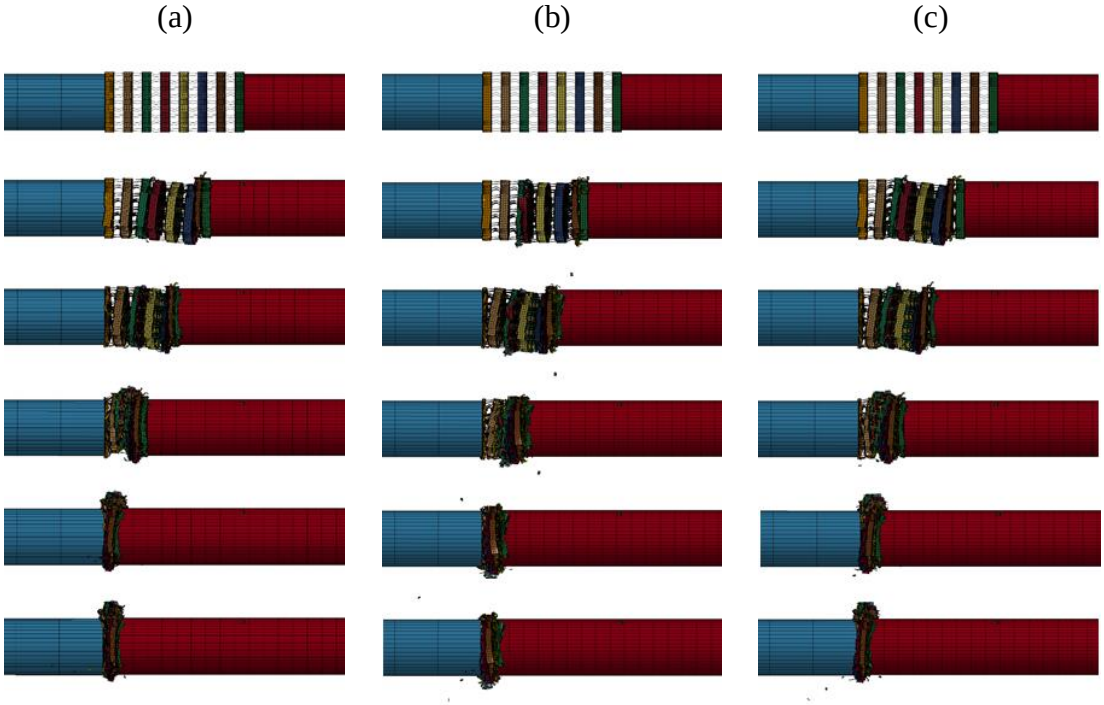

Figure 3.13. The deformation pictures of (a) the material model I, (b) II and (c) III at 0, 600, 1200, 1800, 2400 and 3000 μs (20 m s^{-1})

The distal end and impact end stress-time profiles of the material model I, II and III at 60 m s^{-1} are shown in Figures 3.14(a) and (b), respectively. The distal end initial peak stress increase to 1.63 MPa for the material model I, 2.07 MPa for the material model II, and 2.47 MPa for the material model III when the velocity increases to 60 m s^{-1} when compared with the quasi-static velocity and 20 m s^{-1}, the amount of increase of the initial peak stress and plateau stress is greater. The initial peak stress difference between the material model I (perfect plastic with no strain rate hardening) and material model III (strain hardening with strain rate hardening) is 0.84 MPa. And also the impact end initial peak stresses are 4.76 MPa for the material model I, 4.1 MPa for the material model II and 4.3 MPa for the material model III. As opposite to the quasi-static velocity and 20 m s^{-1}, the impact end stresses of the three material models are very similar to each other at 60 m s^{-1}. The impact end stresses, including initial peak stress and plateau stresses are also higher than the distal end stresses for the three material models as shown in Figures 3.15(a-c), respectively. And the beginning of the stress oscillation can be observed slightly in the same figure.

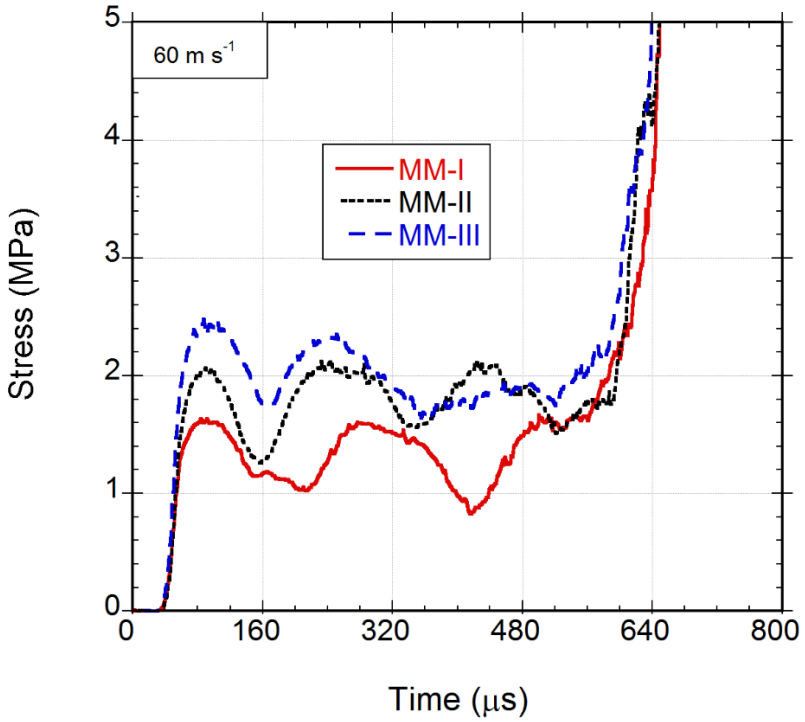

(a)

Figure 3.14. The stress-time curves of the material model I, II and III at 60 m s^{-1}: (a) distal end and (b) impact end

(cont. on next page)

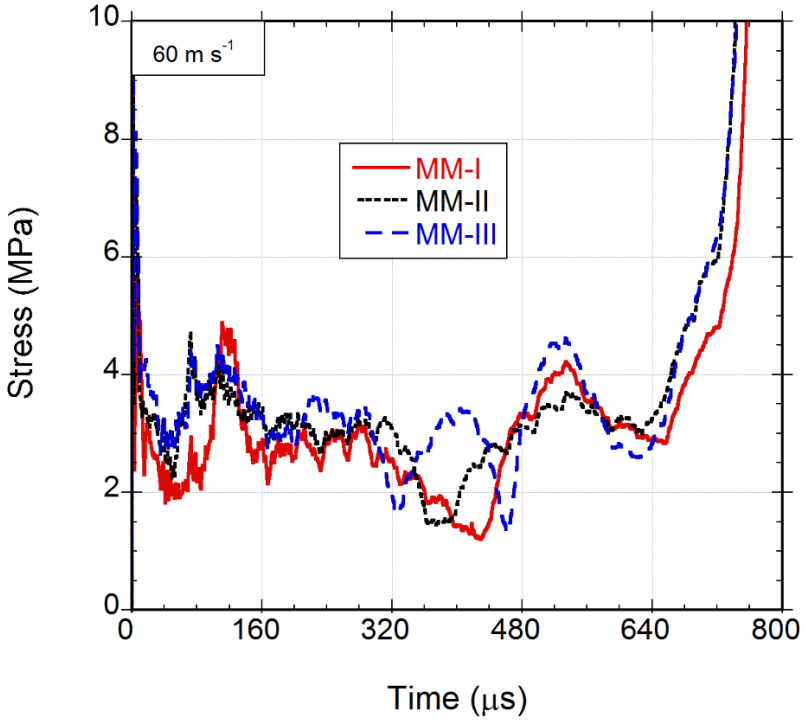

(b)

Figure 3.14 (cont.)

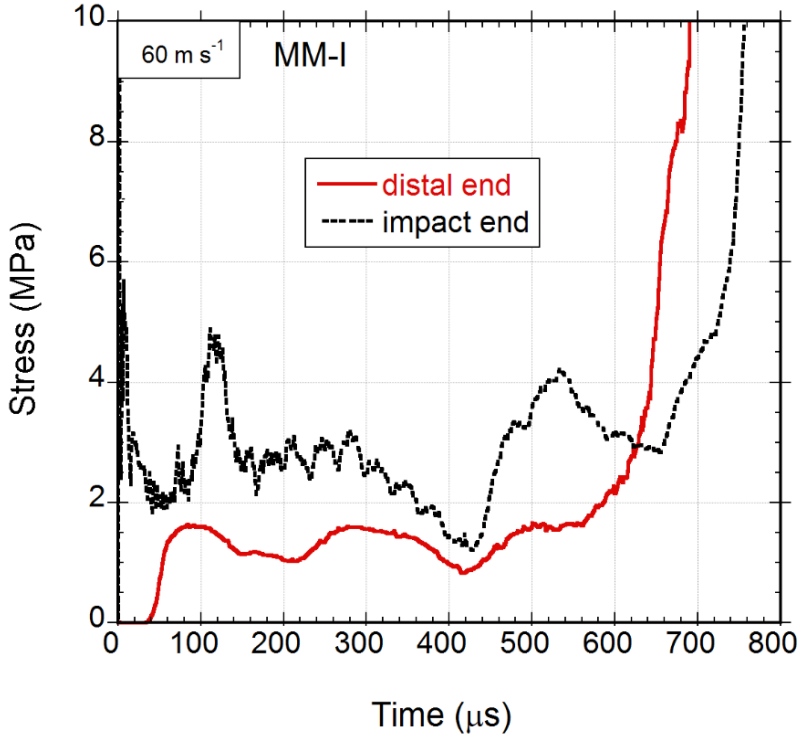

(a)

Figure 3.15. The distal end and impact end stress-time curves of (a) the material model I, (b) II and (c) III at 60 m s^{-1}

(cont. on next page)

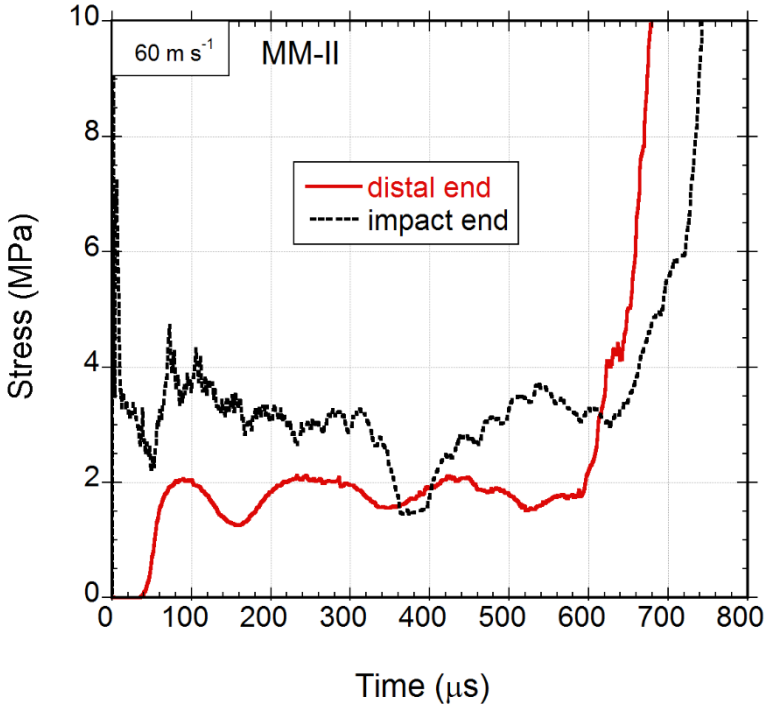

(b)

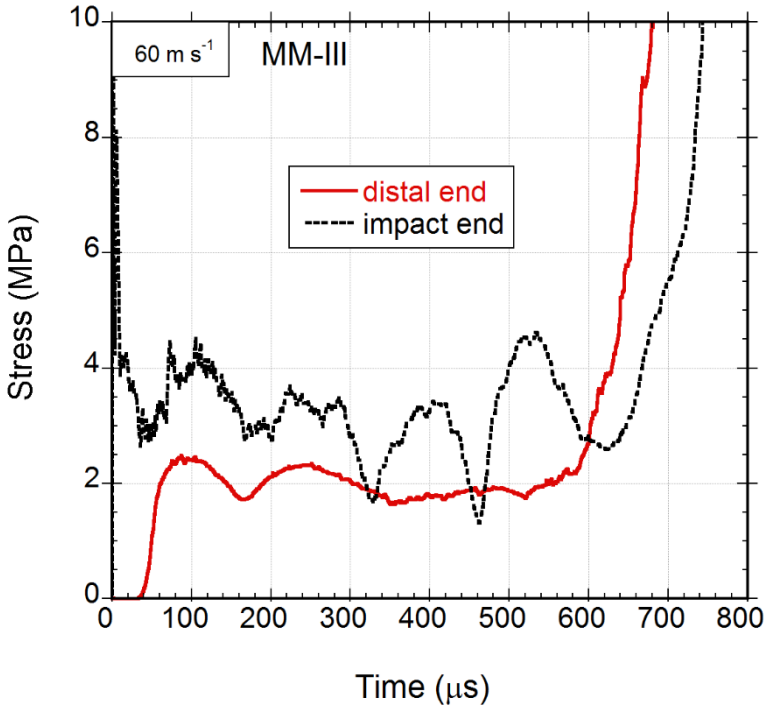

(c)

Figure 3.15 (cont.)

The layer crushing although starts at the impact end; the deformation bands are rather diffusive as can be seen in the deformation pictures at 0, 160, 320, 480, 640 and 800 μs for the three models (Figure 3.16(a-c)).

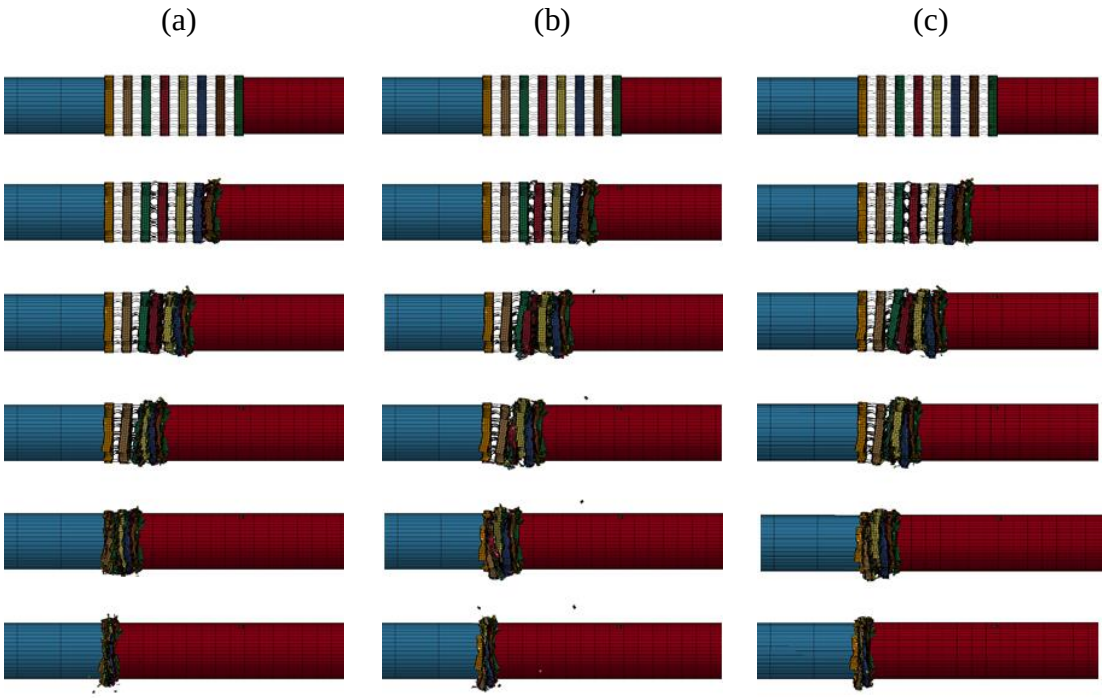

Figure 3.16. The deformation pictures of (a) the material model I (b) II and (c) III at 0, 160, 320, 480, 640 and 800 μs (60 m s^{-1})

The distal end and impact end stress-time profiles of the material model I, material model II and material model III at 150 m s^{-1} are shown in Figures 3.17(a) and (b), respectively. The initial distal end peak stresses are 1.63 MPa for the material model I, 2.1 MPa for the material model II, 2.45 MPa for the material model III. As with the model at 60 m s^{-1}, the three material models impact end stresses are also very similar to each other at 150 m s^{-1}. The impact end stress oscillations for the three material models can be clearly seen in Figure 3.17(b).

The impact end stresses are also higher than the distal end stresses for the three material models as shown in Figures 3.18(a-c), respectively. The impact end initial stresses are 18.75 MPa for the material model I, 13.45 MPa for the material model II and 13.45 MPa for the material model III. The deformation bands at this velocity start at the impact end and proceed sequentially to the distal end showing a shock formation. The deformation pictures of the material model I, II and III can be seen in Figures 3.19(a-c) at 0, 64, 128, 192, 256 and 320 μs.

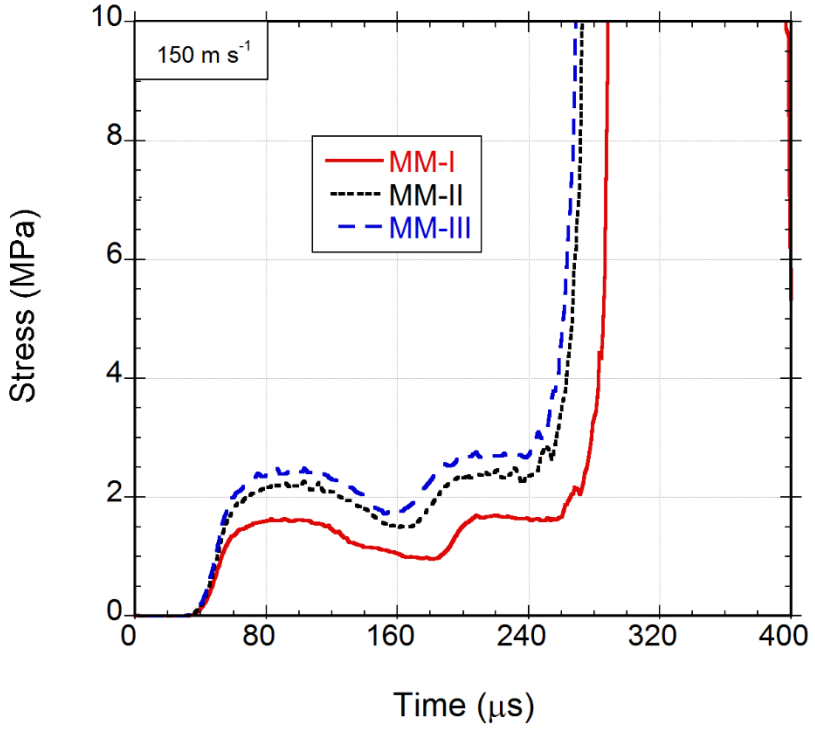

(a)

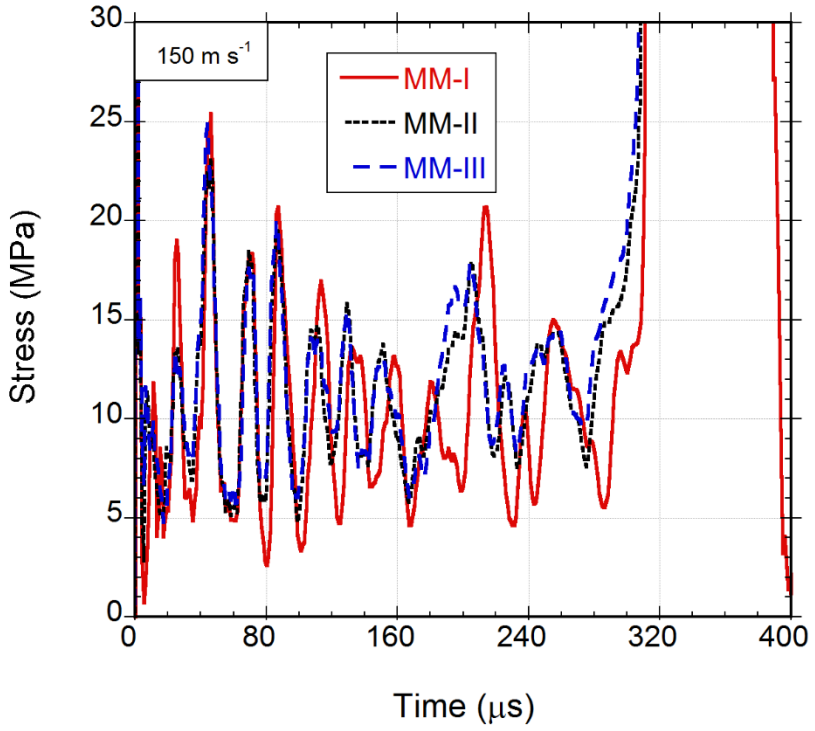

(b)

Figure 3.17. The stress time curves of the material model I, II and III at 150 m s^{-1}: (a) distal end and (b) impact end

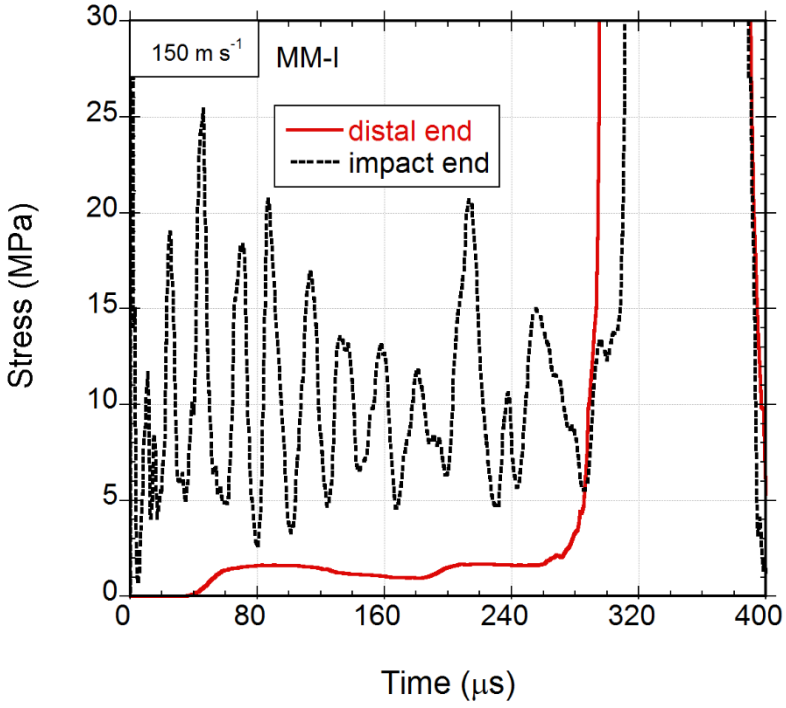

(a)

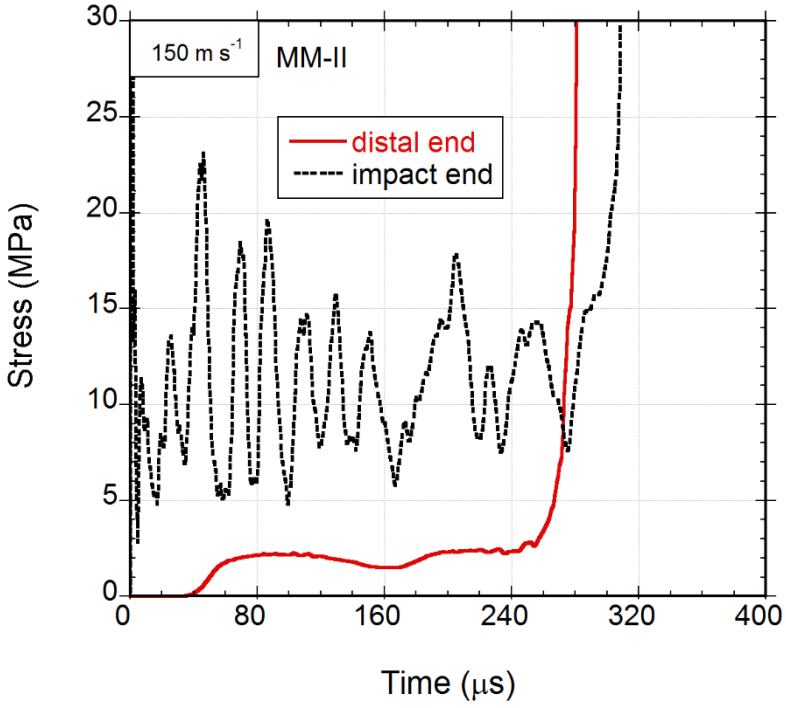

(b)

Figure 3.18. The distal end and impact end stress time curves of the material model (a) I, (b) II and (c) III at 150 m s^{-1}

(cont. on next page)

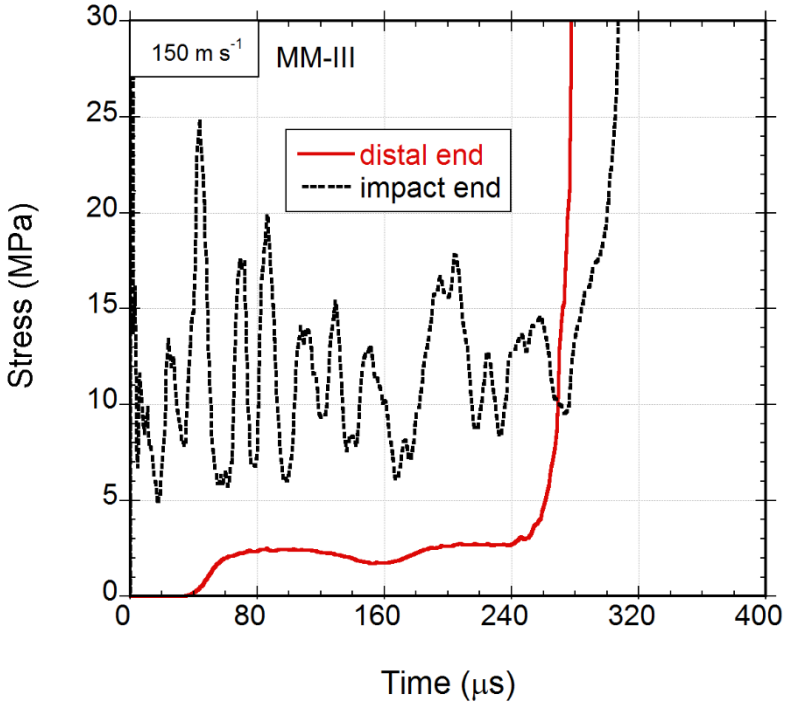

(c)

Figure 3.18 (cont.)

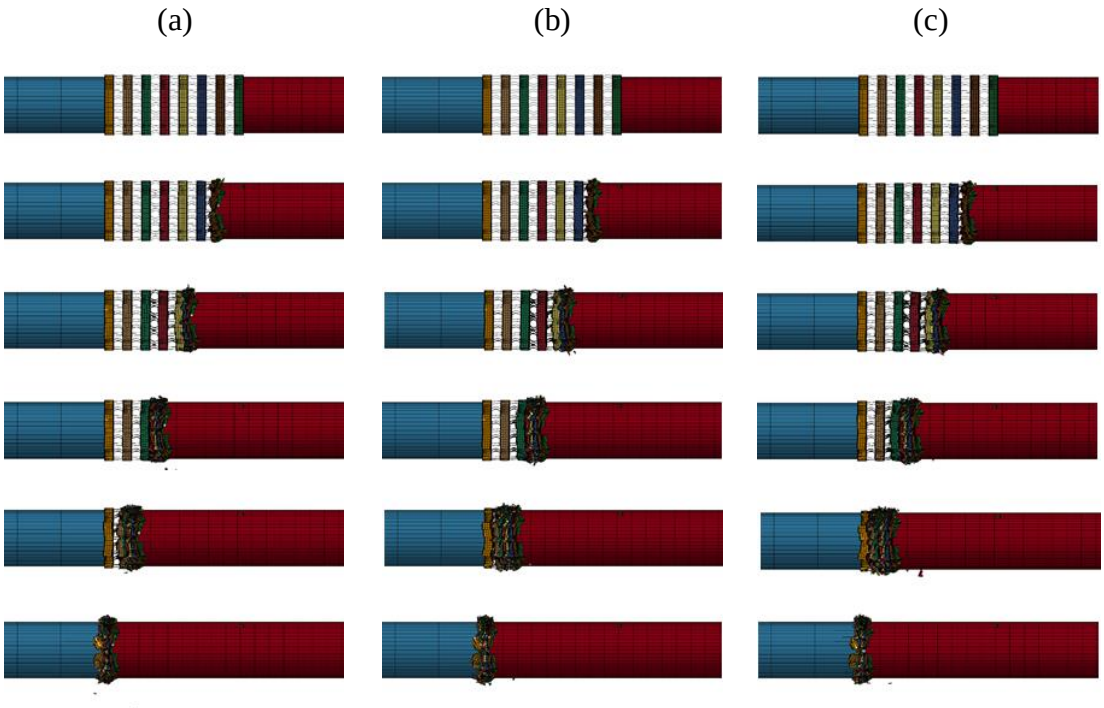

Figure 3.19. The deformation pictures of (a) the model I (b) II and (c) III at 0, 64, 128, 192, 256 and 320 μs (150 m s^{-1})

The impact end and distal end stresses at 250 m s^{-1} are shown in Figures 20(a-c) for the material model I, II and III, respectively. The impact end stresses further increase at this velocity for the material models.

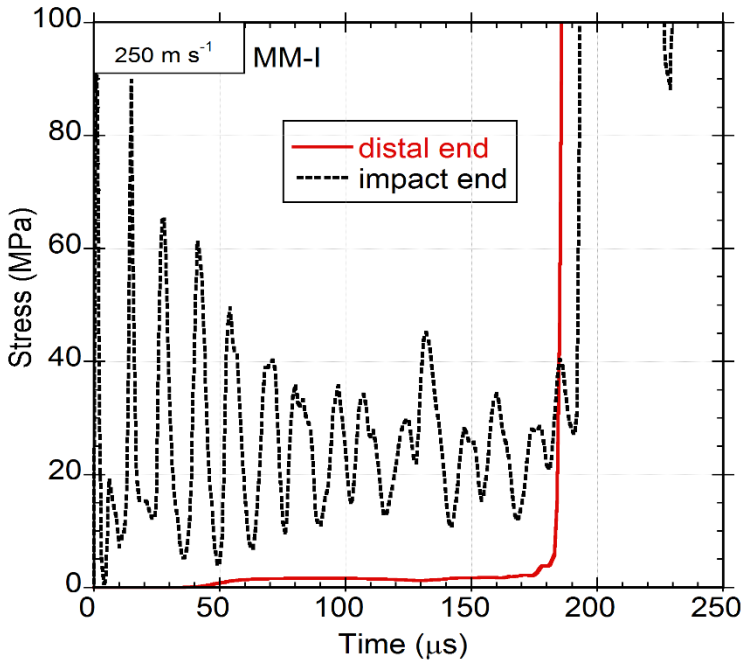

(a)

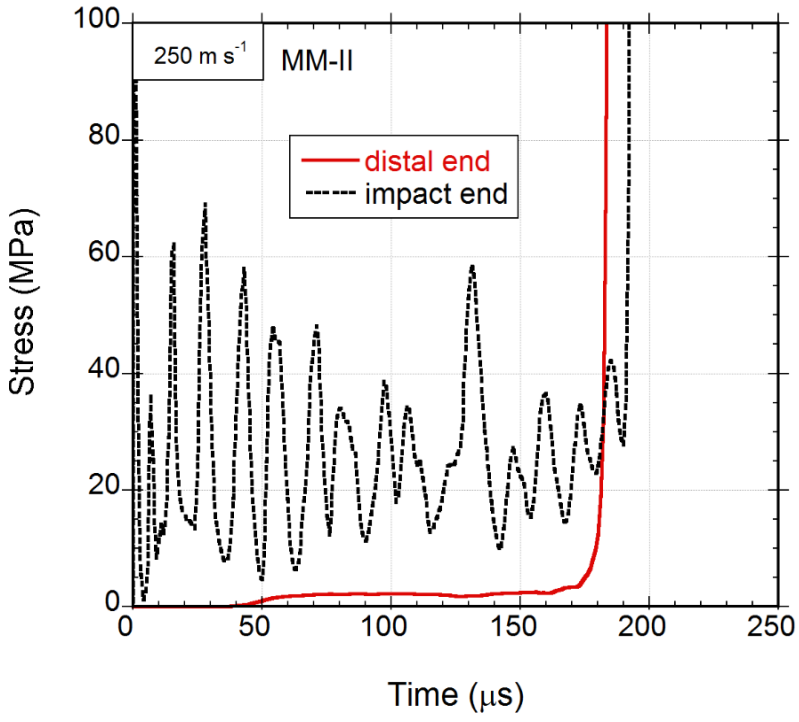

(b)

Figure 3.20. The distal end and impact end stress time curves of (a) the material model I, (b) II and (c) III at 250 m s^{-1}

(cont. on next page)

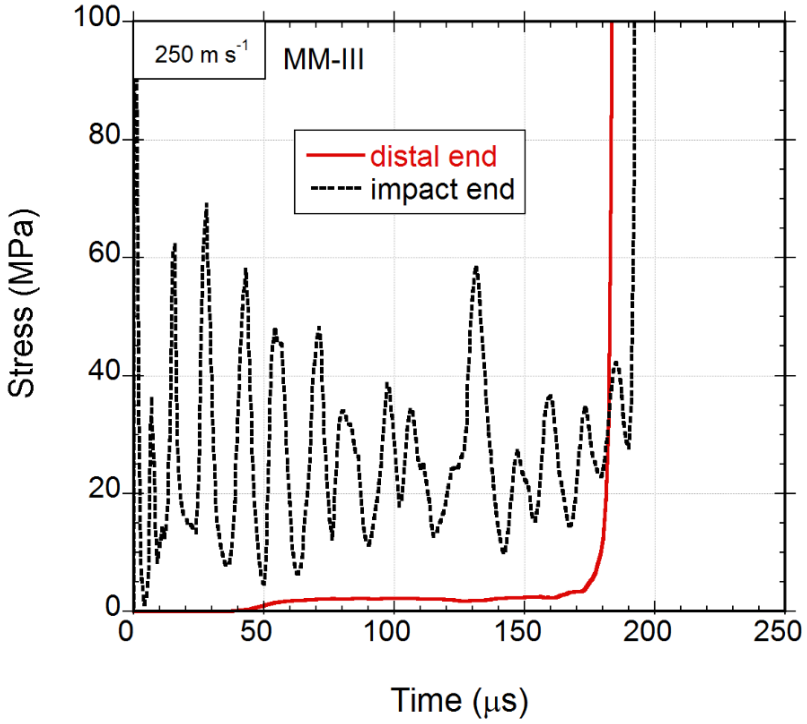

(c)

Figure 3.20. (cont.)

The distal end and impact end stress-strain curves of the material model I are shown in Figures 3.21(a) and (b) at quasi-static and dynamic velocities. As the velocity increases from quasi-static to 20 m s^{-1} and to higher, the distal end stress increases with the reduction of the stress oscillations. It is also noted in Figure 3.21(a) that initial peak stress increases when the velocity increases to 20 m s^{-1}, but it gets nearly a constant values after 20 m s^{-1}. The densification strain is also seen in the same figure decreases as the velocity increases. Although the impact end initial stress at 20 m s^{-1} is higher than that at quasi-static velocity, the post initial peak stress values at both velocities are very much similar to each other as seen in Figure 3.21(b). As the velocity increases to 60, 150 and 250 m s^{-1}, the impact end stress becomes much higher than the quasi-static stress. The stress oscillations also increase significantly with increasing velocity. The oscillation level of the stress is highest at 250 m s^{-1}. The impact end stress densification strain is noted to increase as the velocity increases to 60, 150 and 250 m s^{-1}.

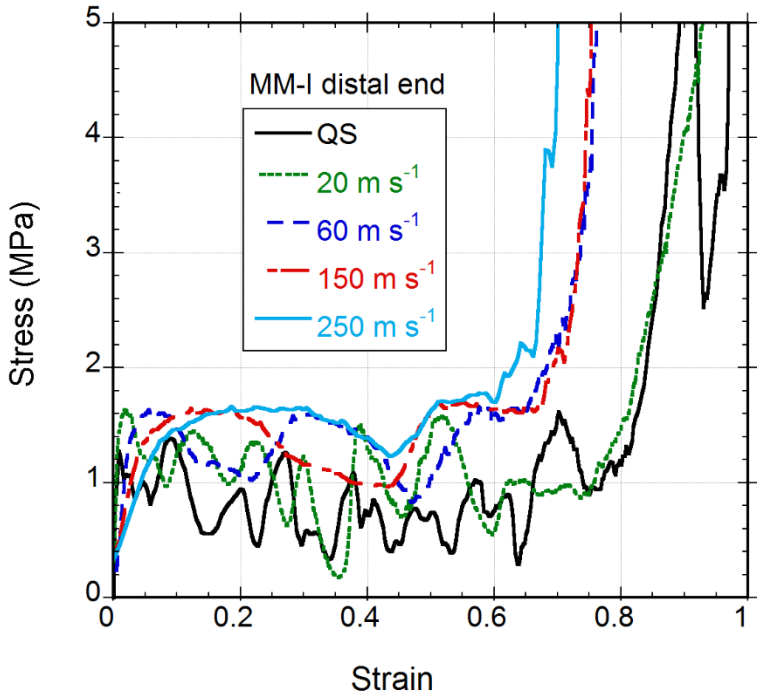

(a)

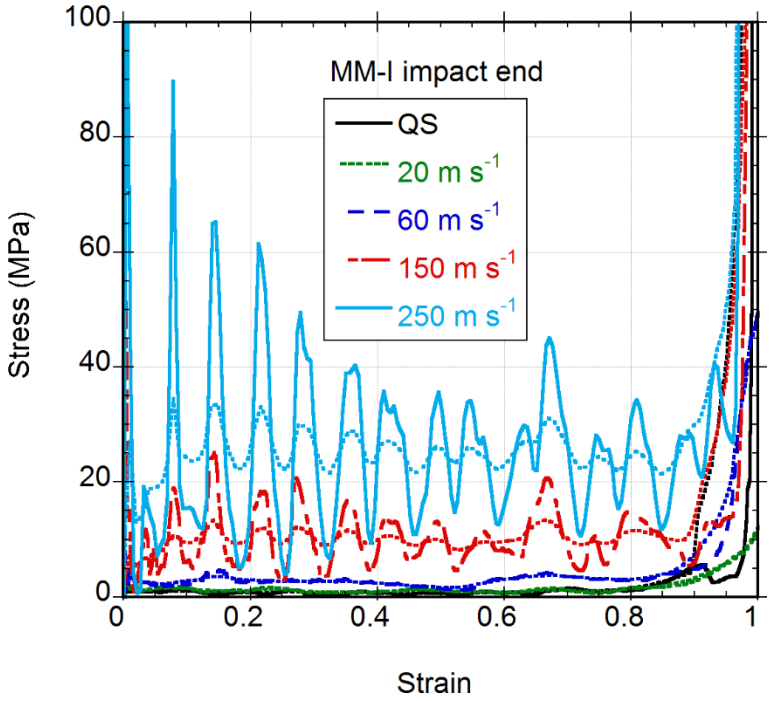

(b)

Figure 3.21. The stress-time curves of the material model I: (a) distal and (b) impact end

Same results are also found in the distal and impact end stress-strain curves of the material model II (Figures 3.22(a) and (b)) and the material model III (Figures 3.23(a) and (b)). Noted that the dotted lines in Figures 3.21(b), 3.22(b) and 3.23(b) represent the

smoothed impact end stresses. For comparison, the impact end stresses at different velocities were then determined from the smoothed curves at a strain of 0.2.

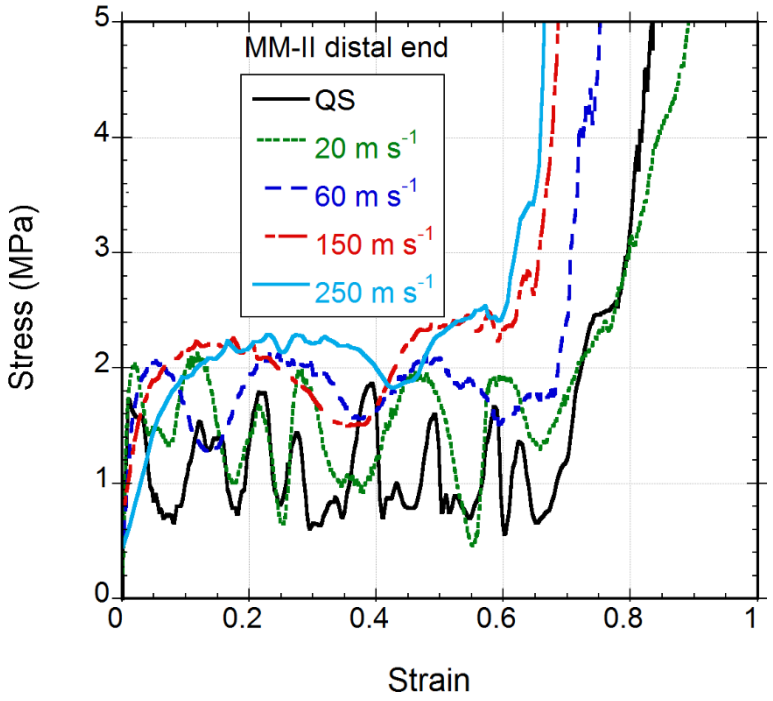

(a)

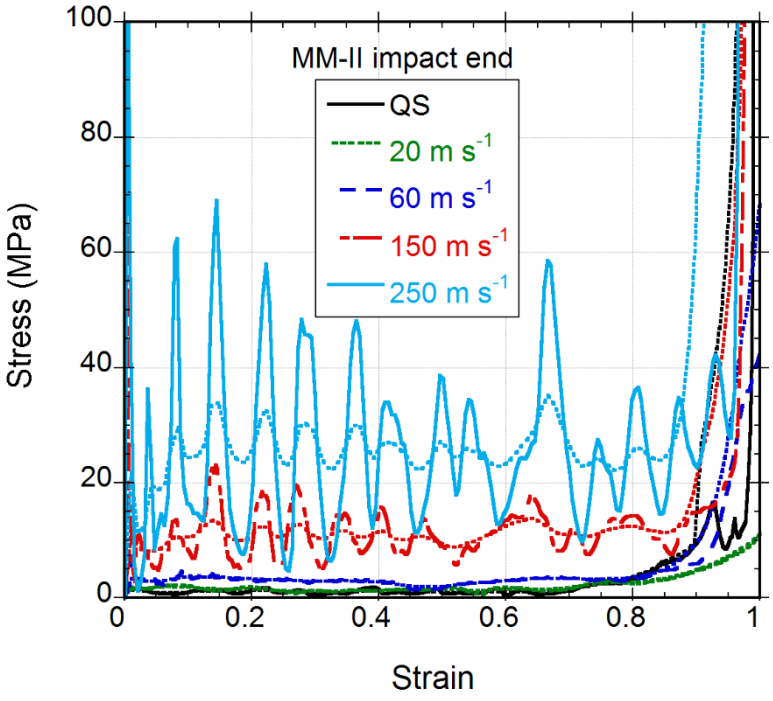

(b)

Figure 3.22. The stress-time curves of the material model II: (a) distal and (b) impact end

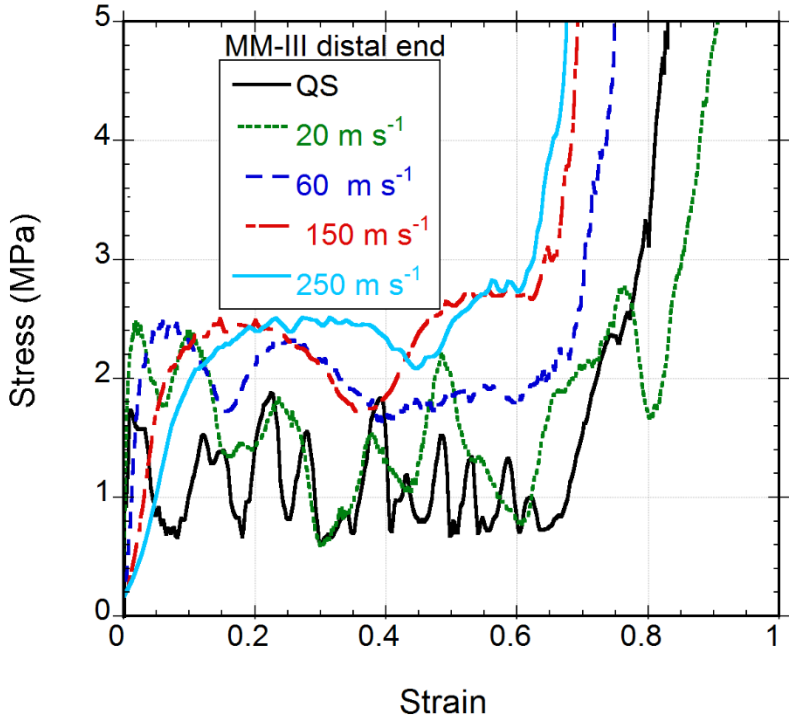

(a)

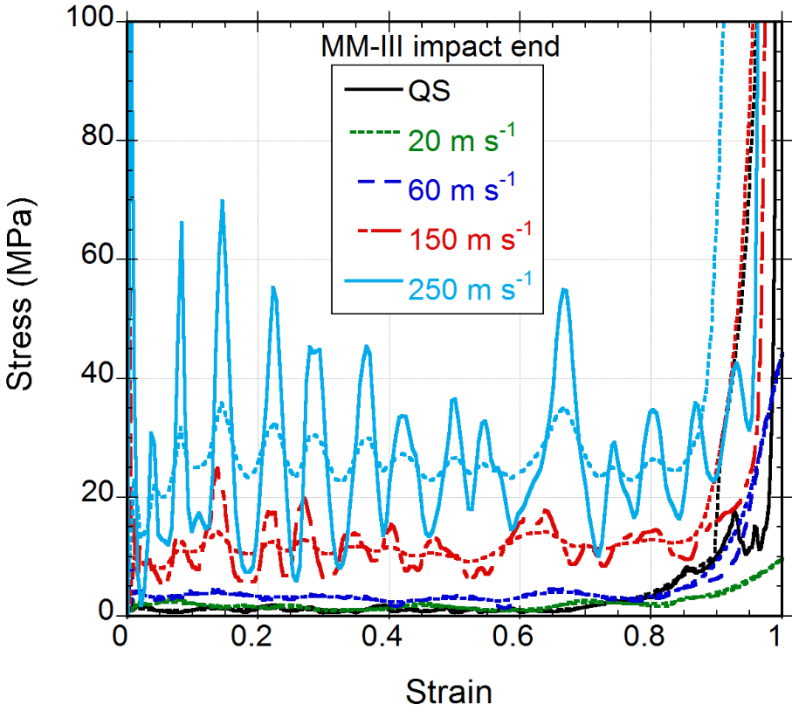

(b)

Figure 3.23. The stress-time curves of the material model III: (a) distal and (b) impact end

Figure 3.24(a-c) show sequentially the distal end stress-time curves of the test and the material model II at 20 and 60 m s^{-1} and the impact end test stress (Taylor impact test) and the material model II impact end stress at 150 m s^{-1}. The deformed pictures of the test samples are also shown in the inset of the same figures. The direct impact and Taylor impact test specimens were 48 mm in length and 19 mm in diameter. The direct impact tests were performed using 25 cm long Inconel bar at ~20 m s^{-1}, 25 cm long aluminum bar at 60 m s^{-1} and 25 cm long wood bar at 90 m s^{-1}. The Taylor impact tests were performed at 150 m s^{-1} by firing the corrugated test specimen directly to the end of the Split Hopkinson Pressure Bar Inconel incident bar having the same diameter with the test sample. The dynamic tests were performed by Sarıkaya in the previous study and the details of the tests were given [51].

The tests and finite element model initial peak stresses (~ 2 MPa) and plateau stresses are almost similar at 20 m s^{-1}, while the finite element model densification strain is lower than the test densification strain as can be seen in Figure 3.24(a). The deformation of the test sample starts at both the impact end and distal end and proceeds non-sequentially as seen in Figure 3.23(a). The center layers of the sample deform at later stages of the deformation. This deformation is very similar to that of the quasi-static velocity. The tests and model initial peak stresses are almost similar at 60 m s^{-1}, ~ 2 MPa (Figure 3.24(b)). Again the finite element model sample densifies at longer time than the test sample. The model and test plateau stresses are also very similar to each other. The deformation starts at the impact end and is nearly planar and sequential as depicted in Figure 3.24(b).

The impact end stresses of the Taylor impact test at 150 m s^{-1} and finite element model impact end stress at 150 m s^{-1} show similar shock stresses as shown in Figure 3.24(c). The deformation starts at the impact end and proceeds sequentially, showing a shock stress formation. In the Taylor impact test, there is a critical mass for the densification of the corrugated sample and below that the sample will not densify. Since no backing mass was used in the test, the sample did not densify. Excluding the densification region, the Taylor impact test stresses show close similarity with the finite element model end test stresses. The oscillations in the stresses simply show the layer wise sequential crushing of the corrugated sample. These results confirm the validity of the used finite element models.

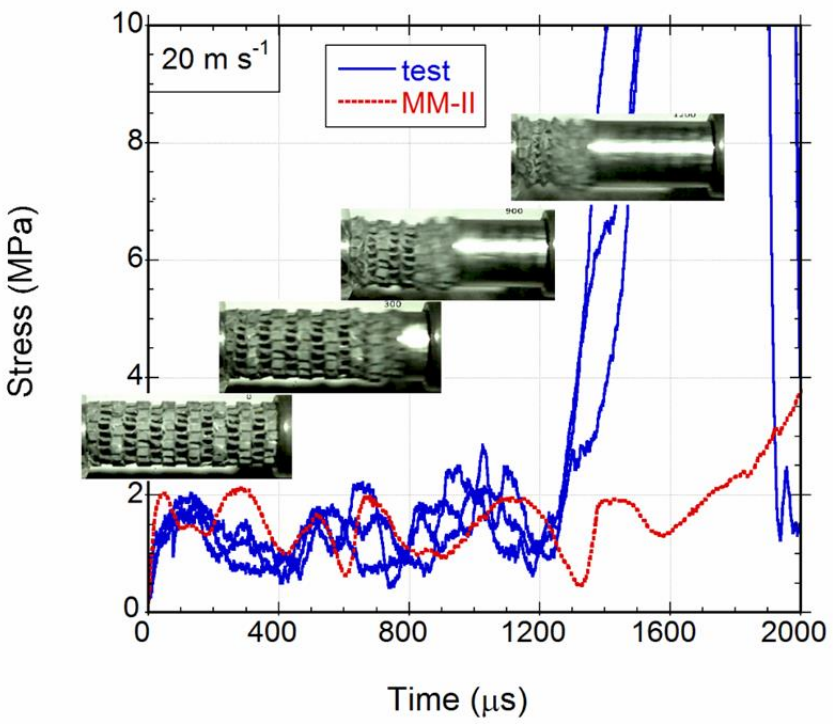

(a)

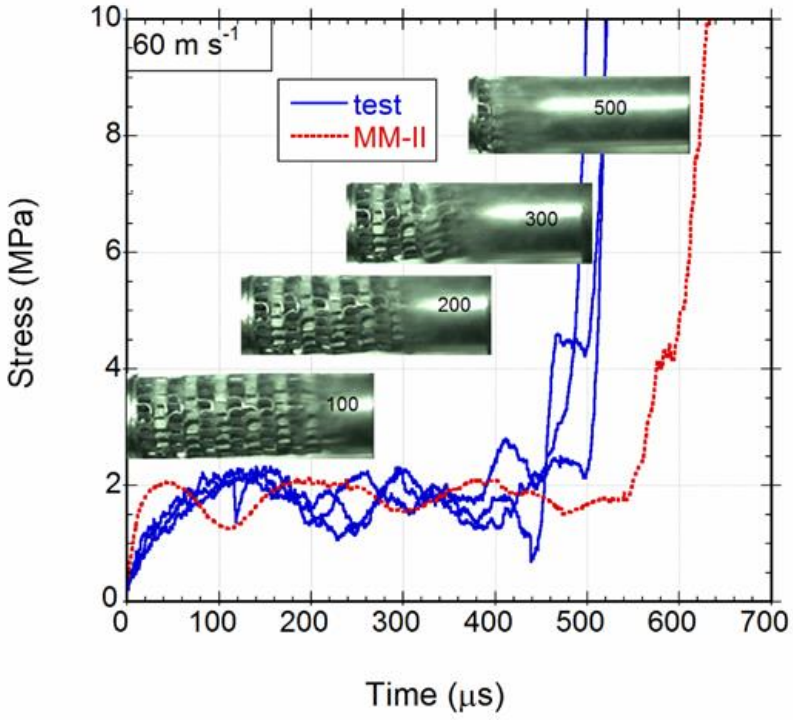

(b)

Figure 3.24. The distal end stress-time curves of the test and the material model II at (a) 20 and (b) 60 m s^{-1} and (c) the impact end test stress (Taylor impact) and model impact end stress at 150 m s^{-1}

(cont. on next page)

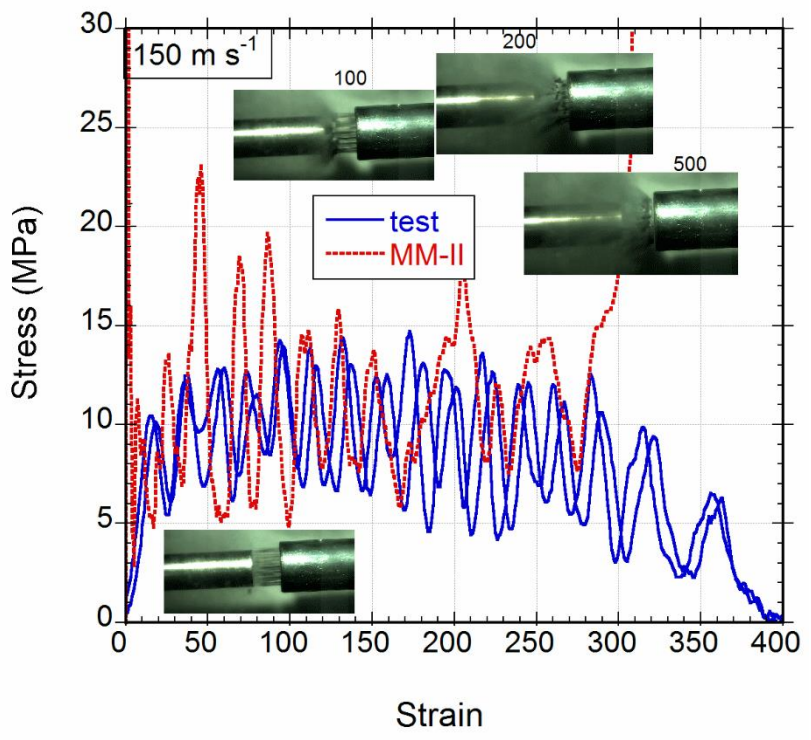

(c)

Figure 3.24 (cont.)

CHAPTER 4

DISCUSSION

4.1. Deformation Modes

The crush bands start to form at the imperfect layers randomly and progresses discretely between 0.0048 and 20 m s^{-1} (Figures 3.10(a-c) and Figures 3.13(a-c)). The numerically calculated impact end and distal end stresses are almost equal to each other and in equilibrium (Figures 3.12(a-c)). This deformation mode is therefore referred as to "quasi-static homogenous mode" [52]. Similar homogenous deformation modes were also reported previously for regular and irregular honeycomb structures [34], Voronoi honeycombs [35], and corrugated layered Al structures [26]. The deformation mode at 60 m s^{-1} is considered as the "transition mode" as the layer crushing is concentrated at the impact end (Figures 3.16(a-c)). Finally, a "shock mode" occurs at 150 and 250 m s^{-1}. In the shock mode, the sample crushes sequentially layer by layer starting at the impact end (Figures 3.19(a-c)). The crushed layer strain in this mode reaches the densification strain or above.

4.2. Layer Strain Histories

Figure 4.1(a-c) shows the imperfect model quasi-static layer strain, nominal strain and stress-time histories of the material model I, II and III. Figure 4.1(d) shows the perfect model quasi-static layer strain, nominal strain and stress-time histories of the material model II. Several important features of quasi-static deformation can be summarized based on the graphs in Figures 4.1(a-c). In all imperfect models, the layer crushing starts at the imperfect 10^{th} layer followed by the crushing of neighboring 9^{th} layer and 8^{th} layer and then the imperfect 2^{nd} layer and neighboring layers. The layer crushing progresses discretely in the imperfect models and two or more layers crush at a time. The single crushing of the layers is expected to result in 15 peak-stresses in the stress-time profile, while the imperfect models result in lesser peak-stress. It is also seen in the same graphs, the layer crushing until the densification strain more or less occurs in two-stage: in the

first the layers crush until about 0.4 strain then in the second the pre-crushed layers are compressed to about 0.8 strain. As noted in Figure 4.1(a), the deformation pattern of the material model I is slightly different from those of other two material models. In this material model, 2nd and 3rd layer crush directly to the densification strain. This two-stage deformation is not seen in the layer-strain history of the perfect model as depicted in Figure 4.1(d). Later it will be shown that the layer crushing in the perfect model starts at the sample's end layers. And the layer crushing progresses more or less in a sequential manner at both ends of sample. As with the imperfect model, the perfect model exhibits the concurrent crushing of two-layers.

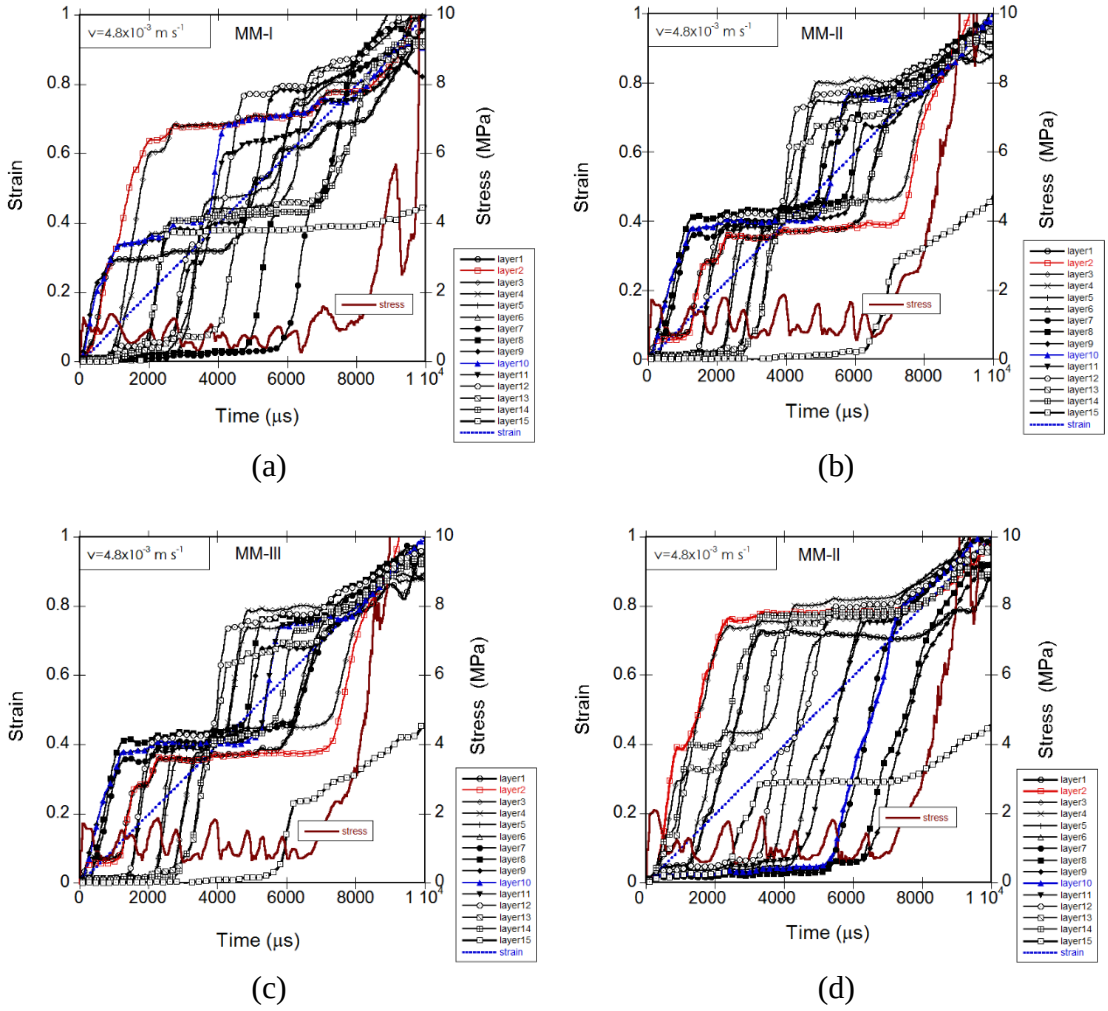

Figure 4.1. The quasi-static layer strain-time, nominal strain-time and distal end stress-time histories of the two-layer double imperfect geometrical model with (a) the material model I, (b) II and (c) III and (d) the perfect model with the material model II

As with quasi-static models, the layer crushing in the imperfect models at 20 m s^{-1} progresses discretely as seen in Figure 4.2(a-c). In contrast to quasi-static models, the layer crushing starts at the imperfect 2nd layer and 1st layer followed by the crushing of the imperfect 10th layer. Collective layer crushing is still continued at this velocity. It is also noted that the extent of stepwise layer deformation is reduced at 20 m s^{-1}: layers crush gradually to 0.6-0.8 strains. In the perfect model, layer crushing again starts at the layer near the ends of the sample (Figure 4.2(d)) and the layer crushing is nearly sequential.

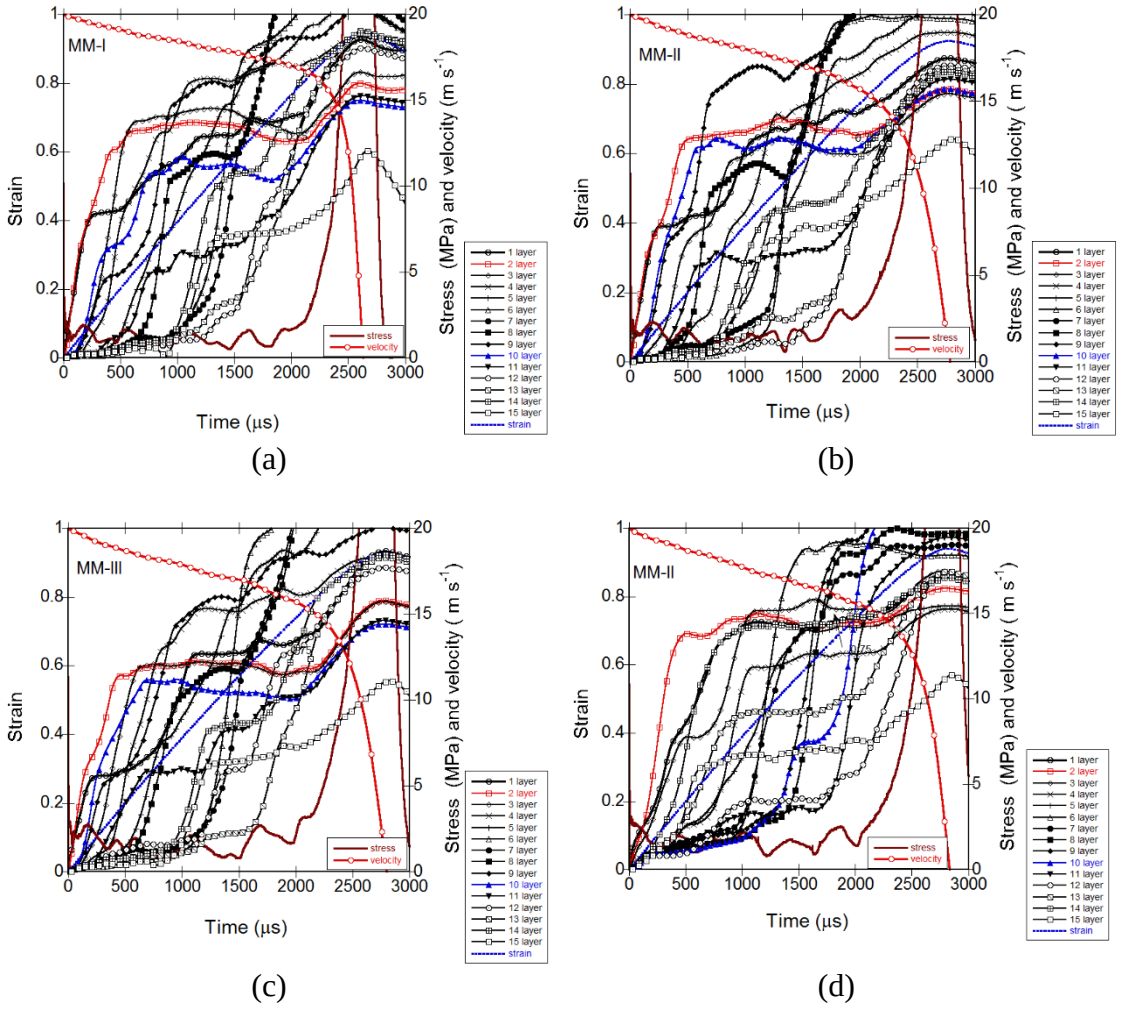

Figure 4.2. The layer strain-time, nominal strain-time and distal end stress-time histories of the two-layer double imperfect geometrical model with (a) the material model I, (b) II and (c) III and (d) perfect model with material model II at 20 m s^{-1}

The layer crushing at 60 m s^{-1} in the imperfect models starts at the impact end. The sequential layer crushing is interrupted by the crushing of the 10^{th} and 9^{th} layers after the crushing of the 5^{th} layer in the material model I and 4^{th} layer in the material models II and III (Figure 4.3(a-c)). Thereafter the crushing of the 10^{th} and 9^{th} layers, the layer crushing switches back to the sequential mode. It is also noted that non-sequential layer crushing starts earlier in the material model II and the material model III than the material model I.

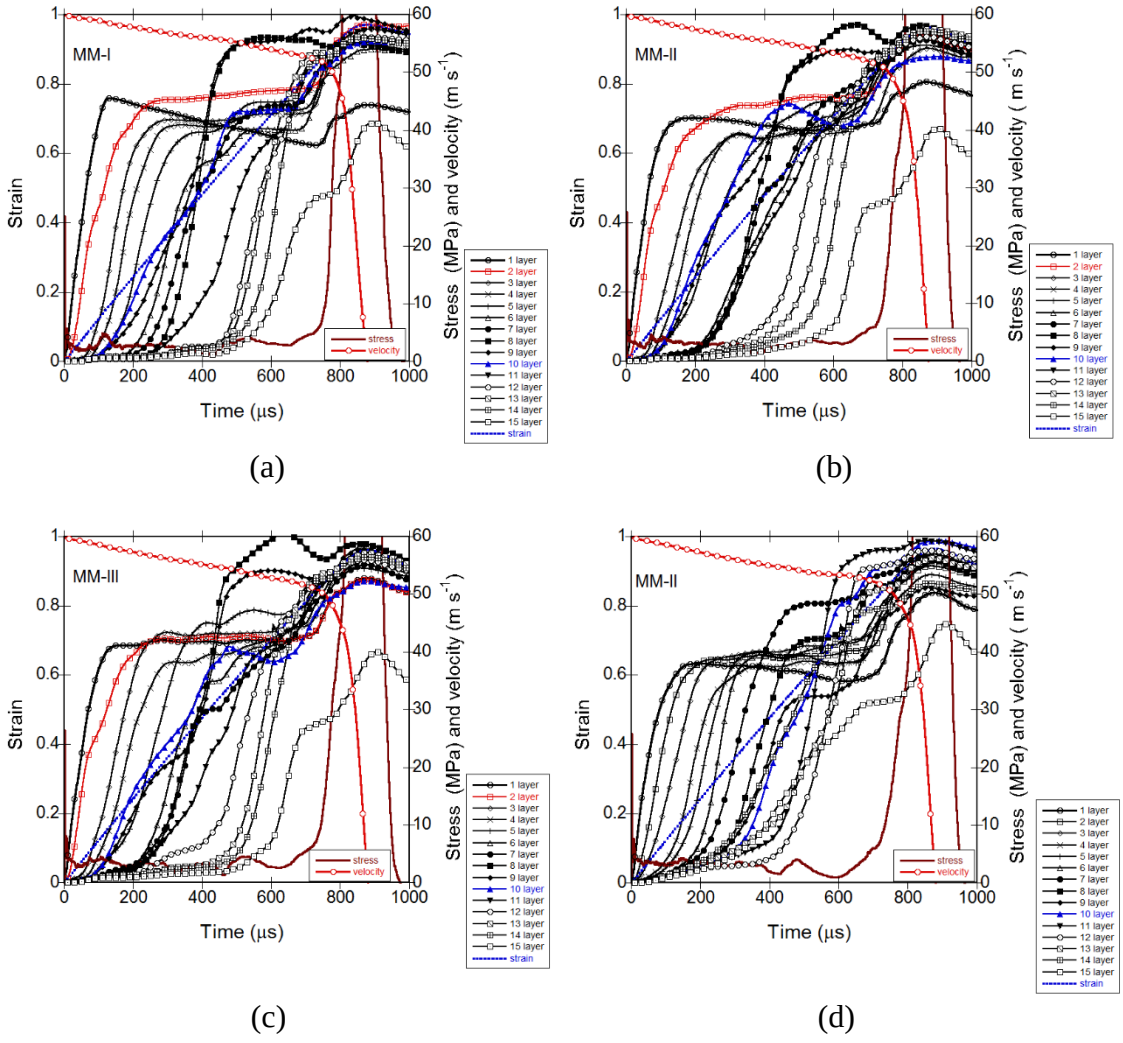

Figure 4.3. The layer strain-time, nominal strain-time and distal end stress-time histories of the two-layer double imperfect geometrical model with (a) the material model I, (b) II and (c) III and (d) perfect model with material model II at 60 m s^{-1}

The strain and strain rate hardening models are tend to induce non-sequential layer crushing. The layers are also crushed until the densification strain, 0.72. The strain distribution in the crush band is wider or diffusive rather than confined in a narrow region.

It is also noted that the collective layer crushing is more pronounced in the material models II and III than the material model I. The layer crushing is sequential until about the crushing of the 9th layer in the perfect model II as seen in Figure 4.3(d) at 60 m s^{-1}. This proves that insertion of imperfect layers delays the shock formation by inducing an early disruption of layer wise collapse. The strain in the crushed layers in the perfect model does not reach the densification strain [52].

When the velocity increases to 150 and 250 m s^{-1}, the layer crushing is completely sequential (Figures 4.4(a-c)) and the layers attain a densification strain of ~0.8. The perfect model also shows a sequential layer crushing at 150 m s^{-1} as seen in Figure 4.4(d).

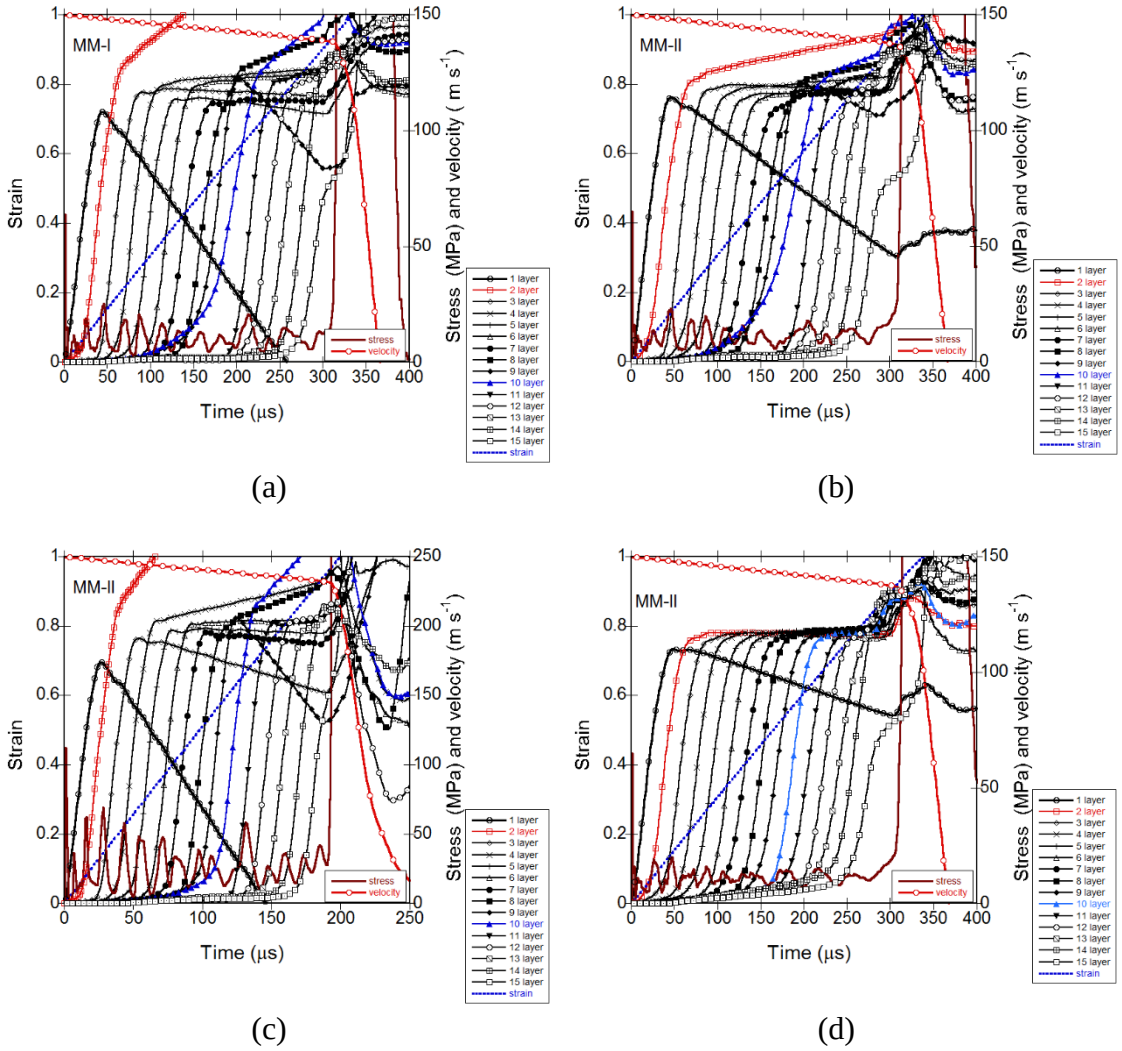

Figure 4.4. The layer strain-time, nominal strain-time and distal end stress-time histories of the two-layer double imperfect geometrical model with (a) the material model I and (b) II at 150 m s^{-1} and (c) the material model II at 250 m s^{-1} and (d) the perfect model with material model II at 150 m s^{-1}

The quasi-static deformation pictures of the perfect model with the material model II are shown in Figure 4.5 at various nominal strains. It is clearly seen in the same figures that the layer crushing starts at both ends of the sample and progresses toward the midsection-layers.

Figure 4.5. The quasi-static deformation pictures of the geometrical perfect model II with the material model II at 0, 0.2, 0.4, 0.6 and 0.8 strains

The deformation sequence of the perfect model with the material model II at 20, 60 and 150 m s^{-1} are shown in Figures 4.6(a-c), respectively. The deformation sequences at these velocities are very similar with those of the imperfect model (material mode II), except the sequential layer crushing is interrupted earlier in the imperfect model. As with the imperfect model, the layer crushing in the perfect model starts at the impact end at all velocities.

Figure 4.6. The deformation pictures of the geometrical perfect model II with the material model II at (a) 20, (b) 60 and (c) 150 m s^{-1}

4.3. Effect of the Insertion of Imperfect Layer on the Crushing Stress

The effects of the insertion of imperfect layers on the distal end stress and impact end stress at quasi-static velocity are seen in Figure 4.7(a). The insertion of two imperfect layers (i) reduces the initial crushing stress, (ii) slightly increases the valley stresses and (iii) has almost no effect on the post-peak stress values and densification strain as compared with the perfect model II. The reduced initial stress of the imperfect model is due to the initiation of the layer crushing at the imperfect layers, while the layer crushing starts at the sample ends in the perfect model. Since the post-peak-stress stress-time histories of the imperfect and perfect model are nearly the same, the densification strain is also the same. As seen in Figure 4.7(a) the distal end stress-time and the impact end stress-time histories of both models are nearly the same at this velocity. The similar effects of the imperfect layer insertion on the distal end and impact end stresses are also seen at 20 m s^{-1} in Figure 4.7 (b). The initial crushing stress is also higher in the perfect model. However, the post peak stresses of both models are nearly the same and the distal end stress-time and the impact end stress-time histories of both models are nearly the same at this velocity. When the velocity increases to 60 m s^{-1}, the impact end stresses of both models become higher than the distal end stresses (Figure 4.7(c)). The distal end initial peak stress of the perfect model, 2.36 MPa, is higher than that of the imperfect model, 2.1 MPa. The reduction of the distal end stress of the imperfect model between 120 and 180 μs in Figure 4.7(c) is due to the collapse of the imperfect and neighboring layers, which tends to transform the shock mode into the quasi-static mode. Initially the impact end stress of the imperfect model is higher and thereafter the impact end stress of the perfect model becomes higher after 100 μs. Nevertheless, the impact end stresses of both models are more or less similar to each other. It is also noted that the densification strains of both models are almost the same at 60 m s^{-1}. When the velocity increases to 150 m s^{-1}, the distal end stresses increase to 2.14 MPa and 2.2 MPa for the perfect and imperfect model, respectively (Figure 4.7(d)). Although the magnitude of stress oscillations increases in both models at150 m s^{-1}, both the perfect and imperfect model end up with the similar impact end stresses and densification strains.

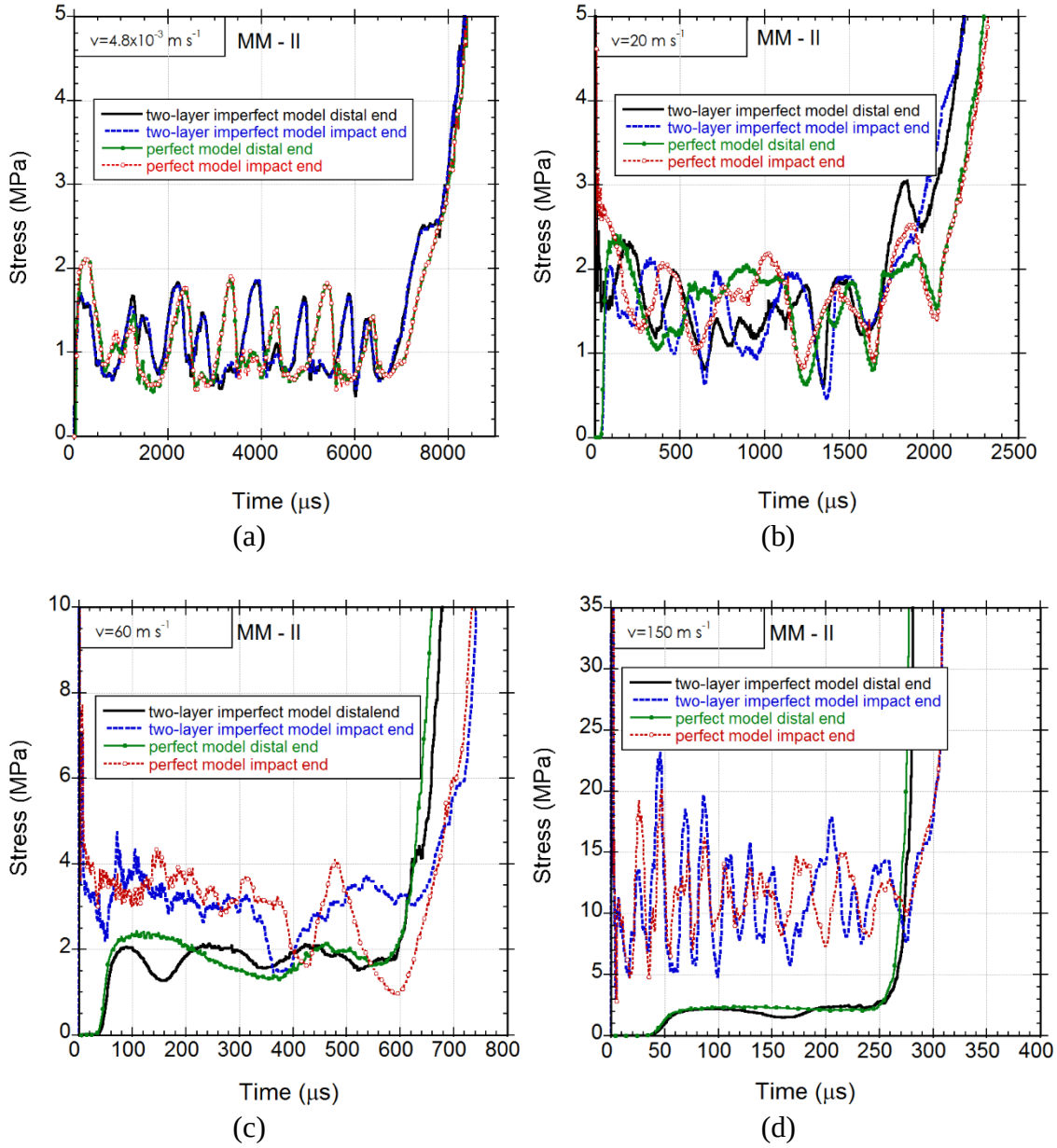

Figure 4.7. The quasi static stress time curves of the two-layer double imperfect model and perfect II model with the material model II: (a) 0.00048, (b) 20, (c) 60 and (d) 150 m s^{-1}

4.4. The Distal End Initial Crushing and Impact End Stresses

The variation of distal end initial crushing stress of the perfect model of the material model II and the imperfect model of the model I, II and III with logarithm of velocity is shown in Figure 4.8(a). The distal end initial crushing stresses increases with increasing logarithm of velocity in both the perfect and imperfect model. The distal end initial crushing stress increases from 1.30, 1.72 and 1.72 MPa at 0.0048 m s^{-1} to 1.6, 2.2 and 2.48 MPa at 150 m s^{-1} for the imperfect model of the model I, II and III, respectively

and within the same velocity range the distal end initial stress of the perfect model of the model II increases from 2.1 MPa to 2.40 MPa as marked with arrows in Figure 4.8(a). The distal end initial crushing stress (σ_p^i) in the same graph is fitted to following equation,

$$\sigma_p^i = \sigma_o + b \ln v \tag{4.1}$$

where σ_o and b are the constants. The fitting results of Eqn.4.1 are further listed in Figure 4.8(a) for the investigated models. The constant b of Eqn. 4.1 is related with the strain rate sensitivity. In Figure 4.8(a), A shows to the increase of the initial crushing stress with the strain hardening, B with the strain rate hardening and C with the perfectness of the geometry. It is noted that the decrease of the initial crushing stress with the insertion imperfect layers decreases as the velocity increases (C). The increase of stress due to the strain hardening (A) and strain rate hardening (B) increases with increasing velocity, while the effect is more pronounced for the strain rate hardening at increasing velocities. The plateau stress in Eqn. 1.3 is taken as the initial crushing stress in Eqn. 4.1 and the based on this the initial peak stress is drawn as function velocity in Figure 4.8(b) using quasi-static and dynamic densification strain of 0.72 and 0.8. It is noted that the r-p-p-l model stress well agrees with the numerical impact end plateau stress (smoothed) at 250 m s^{-1}, while r-p-p-l model with quasi-static densification strain overestimates the numerical plateau stress. By considering all the internal energy was due to the loss of the kinetic energy, the following equation was proposed for the critical velocity (v_{cr}) for the shock formation [39]

$$v_{cr} = \sqrt{\frac{2\sigma_p \varepsilon_d}{\rho_o}} \tag{4.2}$$

Taking σ_p =2 MPa, ρ_o =326 kg m^{-3} and ε_d = 0.8 give a critical velocity of ~100 m s^{-1}. The shock formation also starts at a velocity higher than 60 m s^{-1} as shown in Figure 4.8(b) by a rectangle. Figure 4.8(c) shows the relative increase of the stress with including imperfection, strain and strain rate hardening with velocity. For both impact and distal end stresses, the relative increase is the same and therefore only impact end stress is shown in Figure 4.8(c). For low strain hardening materials, the effect of strain hardening is more significant than the strain rate hardening. Both strain hardening and strain rate hardening effects increase with velocity, while the stress reduction with including

imperfection declines with velocity as the sample starts to deform near the impact end as the velocity increases.

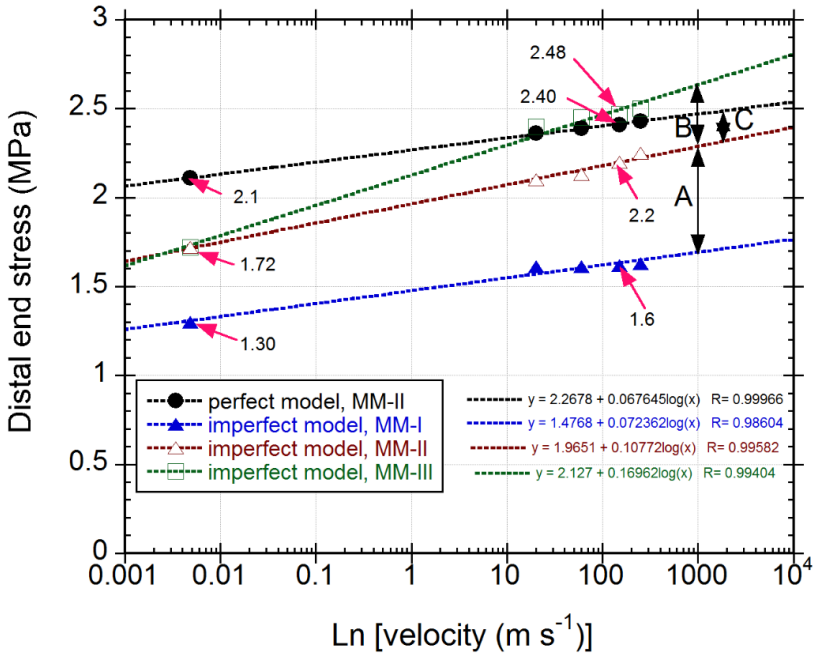

(a)

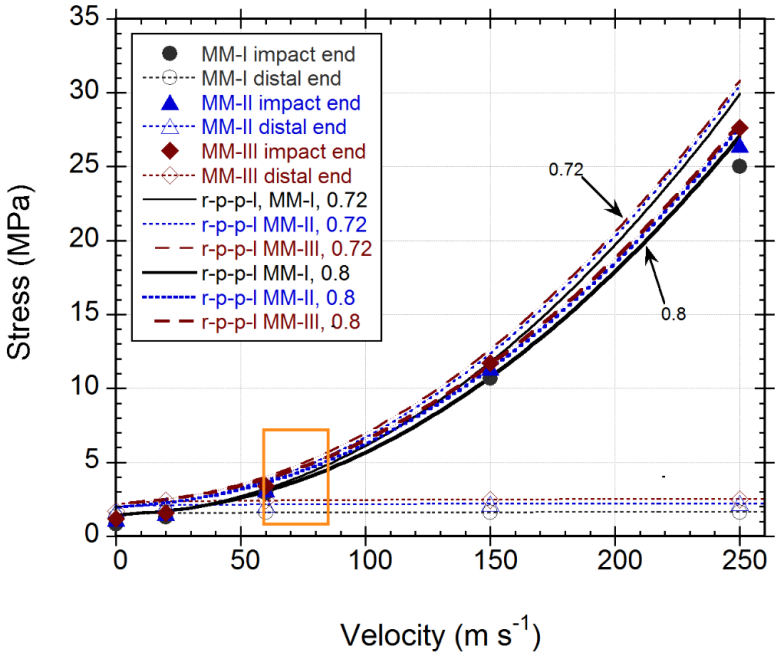

(b)

Figure 4.8. The varation of (a) distal and (b) impact end stresses with velocity and (c) relative increase of the stress with imperfection, strain hardening and strain rate hardening

(cont. on next page)

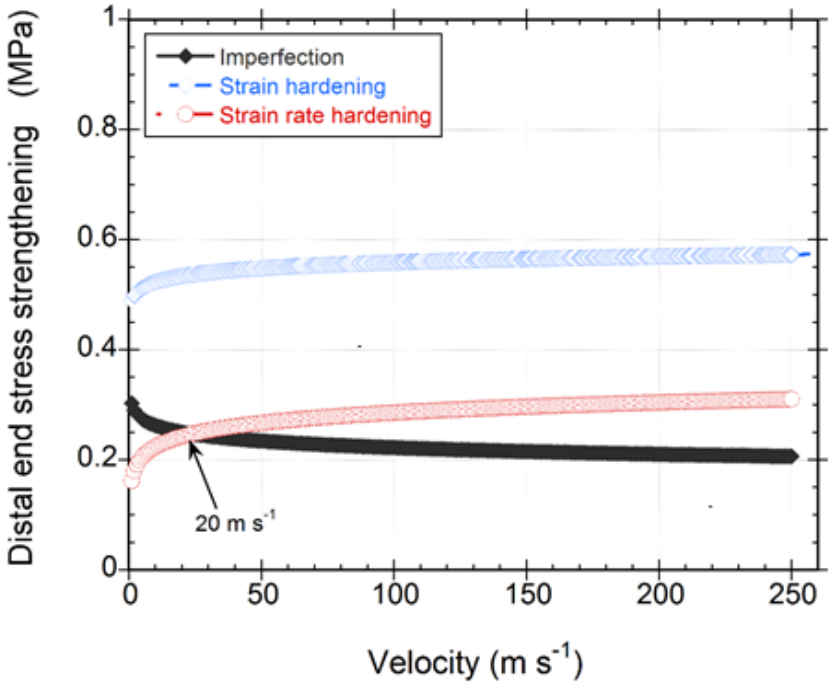

(c)

Figure 4.8. (cont.)

4.5. Nominal and Local Strain Rate

Figure 4.9(a) shows the nominal strain vs. strain of the imperfect simulations of the material model I at different velocities. The nominal strain rates are sequentially 0.1, 400, 1240, 3040 and 5200 s^{-1} for 0.0048, 20, 60, 150 and 250 m s^{-1} velocities. The similar nominal strain rate-strain behavior was also determined for the material model II and III. Figure 4.9(b) shows the 2^{nd}, 5^{th} and 10^{th} layer strain rate variations with the strain for quasi-static imperfect model of the material model I. The 2^{nd}, 5^{th} and 10^{th} layer highest strain rates are 0.75, 0.8 and 0.92 respectively. The dotted line in the same figure shows the nominal strain rate. The layer strain or local strain rate of the perfect 5^{th} layer is 8 times higher than the nominal strain rate. The imperfect 2^{nd} and 10^{th} layers also show similar local strain rate magnification. The highest strain rate is found in the 10^{th} layer, 0.92 s^{-1}. Figure 4.9(c) shows the 5^{th} layer strain rate variation of the perfect model of the material model II and imperfect models of the material model II and III with strain. The 5^{th} layer highest strain rates of the perfect model of material model II, imperfect model of material model II and model III are 0.80, 0.82 and 0.85, respectively. Again the local strain rate is about 8 times of nominal strain rate.

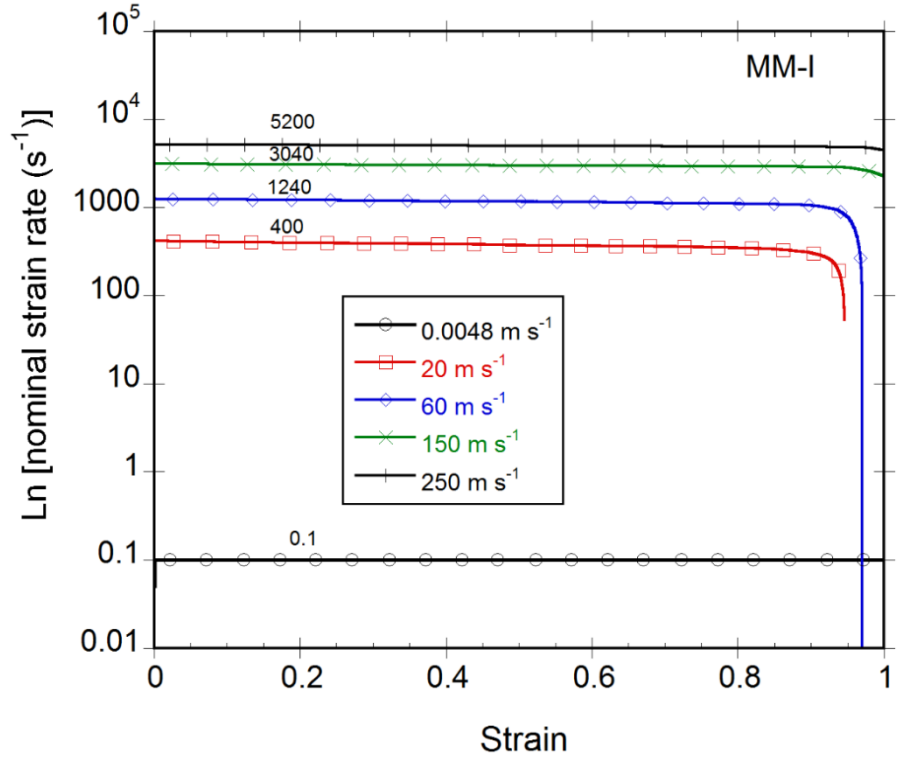

(a)

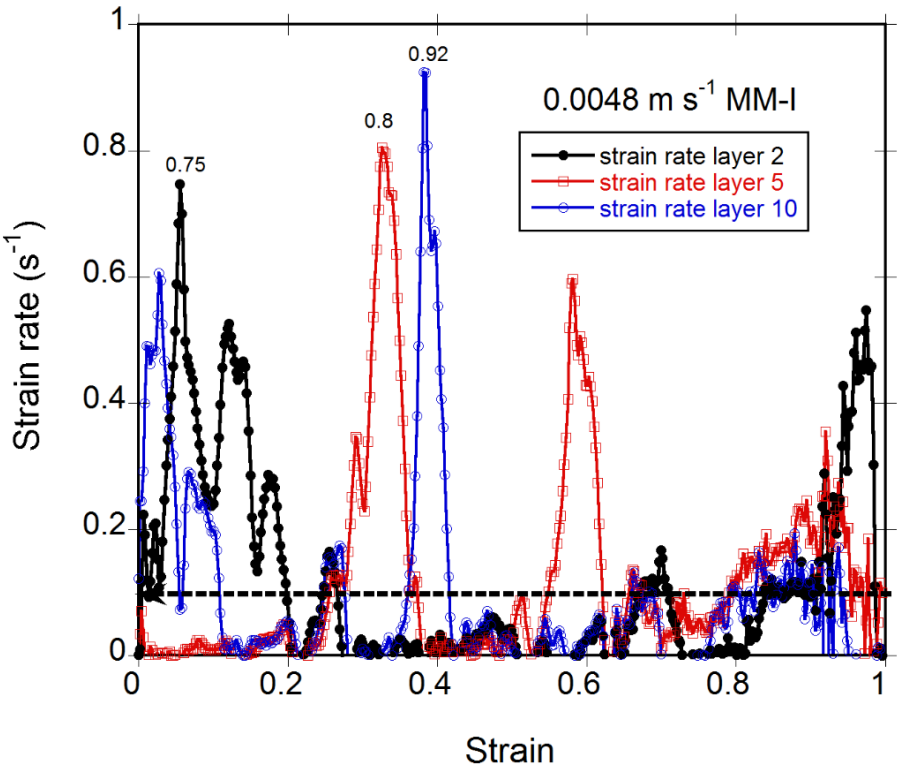

(b)

Figure 4.9. (a) Nominal strain vs. strain at different velocities of imperfect model MM-I and (b) layer strain rates of imperfect model MM-I and (c) the perfect model MM-II and imperfect model MM-II and MM-III

(cont. on next page)

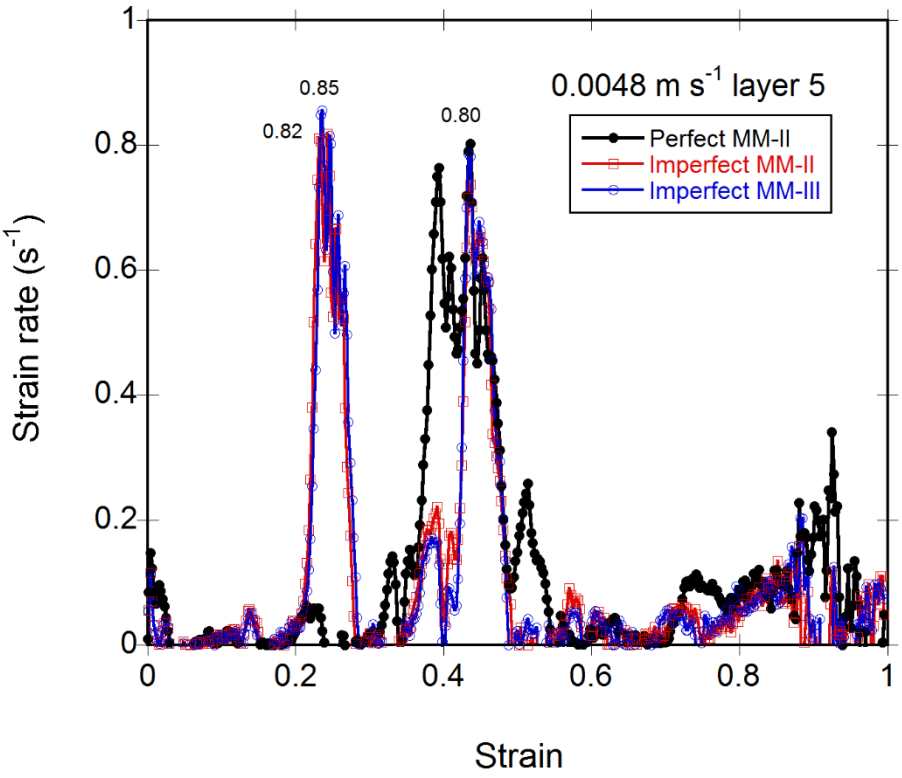

(c)

Figure 4.9. (cont.)

Figure 4.10(a) shows the 2nd layer strain rate-strain variation of the perfect and imperfect models of material model I, model II, model III at 150 m s^{-1}. Nominal strain rate (NSTR) and 2nd layer strain comparison can be seen in the same figure. The 2nd layer highest local strain rates of the imperfect model of material model I, perfect model of material model II and imperfect model of material model III are 26000, 23750 and 22500 s^{-1}, respectively. Figure 4.10(b) shows the 5th and 10th layer strain rate-strain variation of the perfect and imperfect models of material model I, model II and model III at velocity of 150 m s^{-1}. Again the local strain rates are almost 8 times of the nominal strain rate, ~3000 s^{-1}. The reduced strain rate in the 5th and 10th layer is due to the reduced impact velocity with time and layer-wise crushing. The highest local strain rate is found in the imperfect model of the material model I; the local strain rate in this model is 10-15% higher than those of the material model II and material model III. The increase plateau stress with velocity is therefore concluded to be resulted from the strain rate sensitivity of the base material.

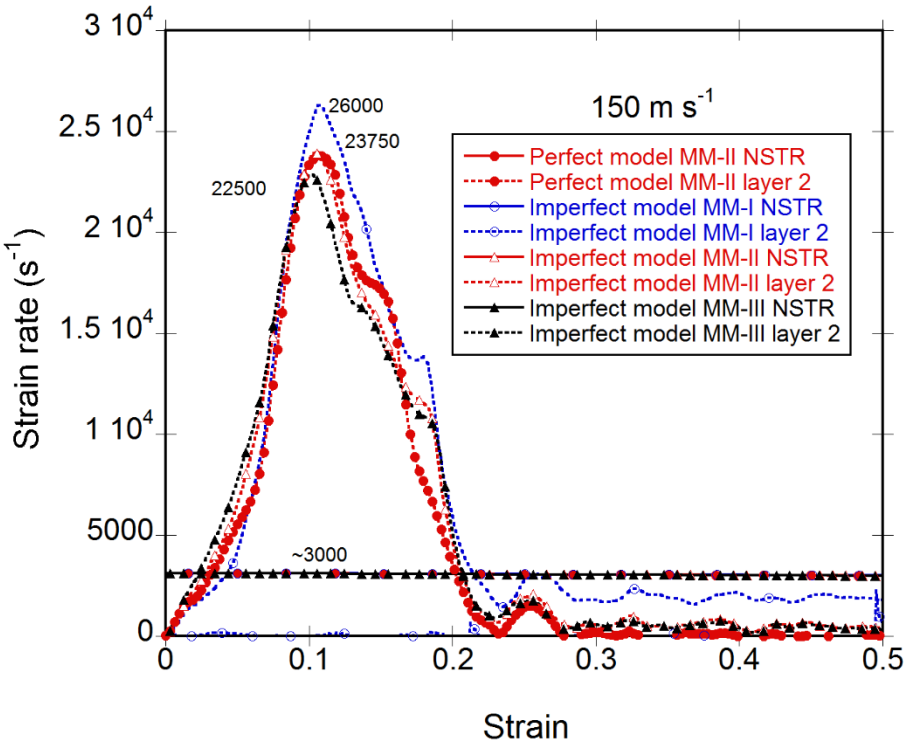

(a)

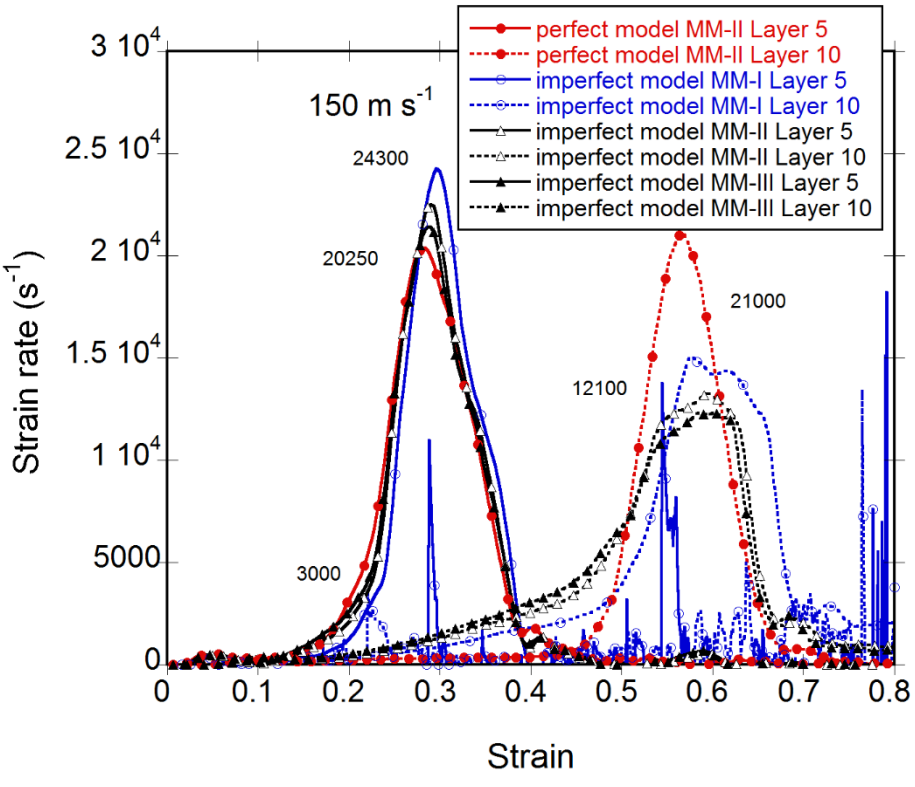

(b)

Figure 4.10. The strain rate vs. strain of (a) 2nd and (b) 5th and 10th layer of perfect and imperfect models

CHAPTER 5

CONCLUSION

The effects of the material models on the crushing behavior of a layered 1050 H14 aluminum corrugated sandwich structure were investigated as function velocity. Three different material models were selected for modelling purpose: elastic perfectly-plastic, elastic-strain hardening and elastic-strain and strain rate hardening. The homogeneous layers of a multi-layered structure with 3D full models allowed to monitor the stress, strain and velocity histories of each layer during the course of deformation. Three-dimensional finite element models were developed in the explicit finite element code of LS-DYNA. The quasi-static compression model was performed at 0.0048 m s^{-1} and the direct impact models were performed at 20, 60, 150 and 250 m s^{-1}. In the modeling of the multilayer corrugated structure, the bent-type imperfect layers were inserted in order to determine the effect of imperfect layers on the crushing behavior.

The crush bands (localized deformation) formed randomly and the initial layer crushing started at the imperfect layers and progressed discretely at the velocities between 0.0048 m s^{-1} and 20 m s^{-1}. Within these velocity range, the numerically calculated stresses at the distal and impact ends were determined almost the same and in equilibrium showing a “quasi-static homogenous mode”. The deformation mode at 60 m s^{-1} was a “transition mode” as the layer crushing was concentrated at the impact end. At 150 and 250 m s^{-1}, the sample crushed in a shock mode in which the layer were collapsed sequentially starting at the impact end and the crushed layer strain in this mode reached the densification strain.

The numerical models showed that the strain and strain rate hardening models tended to induce non-sequential layer crushing. The insertion of imperfect layers delayed the shock formation by inducing an early disruption of layer wise collapse. The collective layer crushing was also more pronounced in the material model II and III than the material model I.

For low strain hardening aluminum and similar materials, the effect of strain hardening in increasing plateau stress was more significant than the strain rate hardening at the quasi-static velocity, while both strain hardening and strain rate hardening effect increased with increasing velocity. The stress reduction with the inclusion of

imperfections declined as the velocity increased since the initial crushing of the samples started near the impact end at increasing velocities.

The layer strain rates were shown to be at least 8 times of the nominal strain rate at both low and high velocities. And, the perfectly elastic plastic model showed the highest local strain rate. The increase in plateau stress with increasing velocity was attributed to the strain rate sensitivity of the base material as it was shown that the impact end stress increased with velocity was almost the same as the increase of the plateau stress.

REFERENCES

[1] Reid, S.R. and C. Peng, *Dynamic uniaxial crushing of wood.* International Journal of Impact Engineering, 1997. 19(5-6): p. 531-570.

[2] Lopatnikov, S.L., et al., *Dynamics of metal foam deformation during Taylor cylinder-Hopkinson bar impact experiment.* Composite Structures, 2003. 61(1-2): p. 61-71.

[3] Harrigan, J.J., et al., *High rate crushing of wood along the grain.* International Journal of Mechanical Sciences, 2005. 47(4-5): p. 521-544.

[4] Karagiozova, D., G.S. Langdon, and G.N. Nurick, *Propagation of compaction waves in metal foams exhibiting strain hardening.* International Journal of Solids and Structures, 2012. 49(19-20): p. 2763-2777.

[5] Alvandi-Tabrizi, Y., et al., *High strain rate behavior of composite metal foams.* Materials Science and Engineering a-Structural Materials Properties Microstructure and Processing, 2015. 631: p. 248-257.

[6] Jung, A., A.D. Pullen, and W.G. Proud, *Strain-rate effects in Ni/Al composite metal foams from quasi-static to low-velocity impact behaviour.* Composites Part a-Applied Science and Manufacturing, 2016. 85: p. 1-11.

[7] Deshpande, V.S. and N.A. Fleck, *High strain rate compressive behaviour of aluminium alloy foams.* International Journal of Impact Engineering, 2000. 24(3): p. 277-298.

[8] Sadot, O., et al., *The trapped gas effect on the dynamic compressive strength of light aluminum foams.* Materials Science and Engineering a-Structural Materials Properties Microstructure and Processing, 2016. 659: p. 278-286.

[9] Tam, L.L. and C.R. Calladine, *INERTIA AND STRAIN-RATE EFFECTS IN A SIMPLE PLATE-STRUCTURE UNDER IMPACT LOADING.* International Journal of Impact Engineering, 1991. 11(3): p. 349-377.

[10] Calladine, C.R. and R.W. English, *STRAIN-RATE AND INERTIA EFFECTS IN THE COLLAPSE OF 2 TYPES OF ENERGY-ABSORBING STRUCTURE.* International Journal of Mechanical Sciences, 1984. 26(11-1): p. 689-&.

[11] Zhao, H., I. Elnasri, and S. Abdennadher, *An experimental study on the behaviour under impact loading of metallic cellular materials.* International Journal of Mechanical Sciences, 2005. 47(4-5): p. 757-774.

[12] Langseth, M. and O.S. Hopperstad, *Static and dynamic axial crushing of square thin-walled aluminium extrusions.* International Journal of Impact Engineering, 1996. 18(7-8): p. 949-968.

[13] Paul, A. and U. Ramamurty, *Strain rate sensitivity of a closed-cell aluminum foam.* Materials Science and Engineering a-Structural Materials Properties Microstructure and Processing, 2000. 281(1-2): p. 1-7.

[14] Tagarielli, V.L., V.S. Deshpande, and N.A. Fleck, *The high strain rate response of PVC foams and end-grain balsa wood.* Composites Part B-Engineering, 2008. 39(1): p. 83-91.

[15] Tilbrook, M.T., et al., *Dynamic crushing of sandwich panels with prismatic lattice cores.* International Journal of Solids and Structures, 2007. 44(18-19): p. 6101-6123.

[16] Barnes, A.T., et al., *Dynamic crushing of aluminum foams: Part I - Experiments.* International Journal of Solids and Structures, 2014. 51(9): p. 1631-1645.

[17] Tan, P.J., et al., *Dynamic compressive strength properties of aluminium foams. Part I - experimental data and observations.* Journal of the Mechanics and Physics of Solids, 2005. 53(10): p. 2174-2205.

[18] Zou, Z., et al., *Dynamic crushing of honeycombs and features of shock fronts.* International Journal of Impact Engineering, 2009. 36(1): p. 165-176.

[19] Chen, A., et al., *Non-explosive simulated blast loading of balsa core sandwich composite beams.* Composite Structures, 2011. 93(11): p. 2768-2784.

[20] Wang, S.L., et al., *Dynamic material parameters of closed-cell foams under high-velocity impact.* International Journal of Impact Engineering, 2017. 99: p. 111-121.

[21] Liu, H., et al., *Theoretical investigation on impact resistance and energy absorption of foams with nonlinearly varying density.* Composites Part B-Engineering, 2017. 116: p. 76-88.

[22] Zhang, B.Y., et al., *Quasi-static and high strain rates compressive behavior of aluminum matrix syntactic foams.* Composites Part B-Engineering, 2016. 98: p. 288-296.

[23] Liu, H., et al., *Effect of elastic target on Taylor-Hopkinson impact of low-density foam material.* International Journal of Impact Engineering, 2016. 94: p. 109-119.

[24] Elnasri, I., et al., *Shock enhancement of cellular structures under impact loading: Part I experiments.* Journal of the Mechanics and Physics of Solids, 2007. 55(12): p. 2652-2671.

[25] Liu, H., et al., *Performance of aluminum foam–steel panel sandwich composites subjected to blast loading.* Materials & Design, 2013. 47(0): p. 483-488.

[26] Odac, I.K., et al., *The varying densification strain in a multi-layer aluminum corrugate structure: Direct impact testing and layer-wise numerical modelling.* International Journal of Impact Engineering, 2017. 103: p. 64-75.

[27] Tan, P.J., S.R. Reid, and J.J. Harrigan, *On the dynamic mechanical properties of open-cell metal foams - A re-assessment of the 'simple-shock theory'.* International Journal of Solids and Structures, 2012. 49(19-20): p. 2744-2753.

[28] Gaitanaros, S. and S. Kyriakides, *Dynamic crushing of aluminum foams: Part II - Analysis.* International Journal of Solids and Structures, 2014. 51(9): p. 1646-1661.

[29] Sun, Y.L. and Q.M. Li, *Dynamic compressive behaviour of cellular materials: A review of phenomenon, mechanism and modelling.* International Journal of Impact Engineering, 2018. 112: p. 74-115.

[30] Wu, E. and W.S. Jiang, *Axial crush of metallic honeycombs.* International Journal of Impact Engineering, 1997. 19(5-6): p. 439-456.

[31] Zhao, H. and G. Gary, *Crushing behaviour of aluminium honeycombs under impact loading.* International Journal of Impact Engineering, 1998. 21(10): p. 827-836.

[32] Harrigan, J.J., S.R. Reid, and C. Peng, *Inertia effects in impact energy absorbing materials and structures.* International Journal of Impact Engineering, 1999. 22(9-10): p. 955-979.

[33] Tao, Y., et al., *Strain rate effect on the out-of-plane dynamic compressive behavior of metallic honeycombs: Experiment and theory.* Composite Structures, 2015. 132: p. 644-651.

[34] Zheng, Z.J., J.L. Yu, and J.R. Li, *Dynamic crushing of 2D cellular structures: A finite element study.* International Journal of Impact Engineering, 2005. 32(1-4): p. 650-664.

[35] Liu, Y.D., et al., *A numerical study on the rate sensitivity of cellular metals.* International Journal of Solids and Structures, 2009. 46(22-23): p. 3988-3998.

[36] Honig, A. and W.J. Stronge, *In-plane dynamic crushing of honeycomb. Part I: crush band initiation and wave trapping.* International Journal of Mechanical Sciences, 2002. 44(8): p. 1665-1696.

[37] Hall, I.W., M. Guden, and C.J. Yu, *Crushing of aluminum closed cell foams: Density and strain rate effects.* Scripta Materialia, 2000. 43(6): p. 515-521.

[38] Radford, D.D., V.S. Deshpande, and N.A. Fleck, *The use of metal foam projectiles to simulate shock loading on a structure.* International Journal of Impact Engineering, 2005. 31(9): p. 1152-1171.

[39] Tan, P.J., et al., *Dynamic compressive strength properties of aluminium foams. Part II - 'shock' theory and comparison with experimental data and numerical models.* Journal of the Mechanics and Physics of Solids, 2005. 53(10): p. 2206-2230.

[40] Zhao, H., I. Elnasri, and H.J. Li, *The mechanism of strength enhancement under impact loading of cellular materials.* Advanced Engineering Materials, 2006. 8(9): p. 877-883.

[41] Pattofatto, S., et al., *Shock enhancement of cellular structures under impact loading: Part II analysis.* Journal of the Mechanics and Physics of Solids, 2007. 55(12): p. 2672-2686.

[42] Wang, P.F., et al., *Experimental investigation on the strain-rate effect and inertia effect of closed-cell aluminum foam subjected to dynamic loading.* Materials Science and Engineering a-Structural Materials Properties Microstructure and Processing, 2015. 620: p. 253-261.

[43] Qiao, J.X. and C.Q. Chen, *In-plane crushing of a hierarchical honeycomb.* International Journal of Solids and Structures, 2016. 85-86: p. 57-66.

[44] Kilicaslan, C., I.K. Odaci, and M. Gueden, *Single- and double-layer aluminum corrugated core sandwiches under quasi-static and dynamic loadings.* Journal of Sandwich Structures & Materials, 2016. 18(6): p. 667-692.

[45] Kilicaslan, C., et al., *The impact responses and the finite element modeling of layered trapezoidal corrugated aluminum core and aluminum sheet interlayer sandwich structures.* Materials & Design, 2013. 46: p. 121-133.

[46] Kilicaslan, C., et al., *Experimental and numerical studies on the quasi-static and dynamic crushing responses of multi-layer trapezoidal aluminum corrugated sandwiches.* Thin-Walled Structures, 2014. 78: p. 70-78.

[47] Heimbs, S., *Virtual testing of sandwich core structures using dynamic finite element simulations.* Computational Materials Science, 2009. 45(2): p. 205-216.

[48] Asprone, D., et al., *Statistical finite element analysis of the buckling behavior of honeycomb structures.* Composite Structures, 2013. 105: p. 240-255.

[49] Lee, S., et al., *Dynamic failure of metallic pyramidal truss core materials - Experiments and modeling.* International Journal of Plasticity, 2006. 22(11): p. 2118-2145.

[50] Meyers, M.A., *Plastic Deformation at High Strain Rates*, in *Dynamic Behavior of Materials*. 1994. p. 325-330.

[51] Sarikaya, M., M. Guden, and A. Tasdemirci, *The deformation behavior of a multi-layered aluminum corrugated structure at increasing velocities*. 2017.

[52] Zheng, Z.J., et al., *Dynamic crushing of cellular materials: Continuum-based wave models for the transitional and shock modes.* International Journal of Impact Engineering, 2012. 42: p. 66-79.